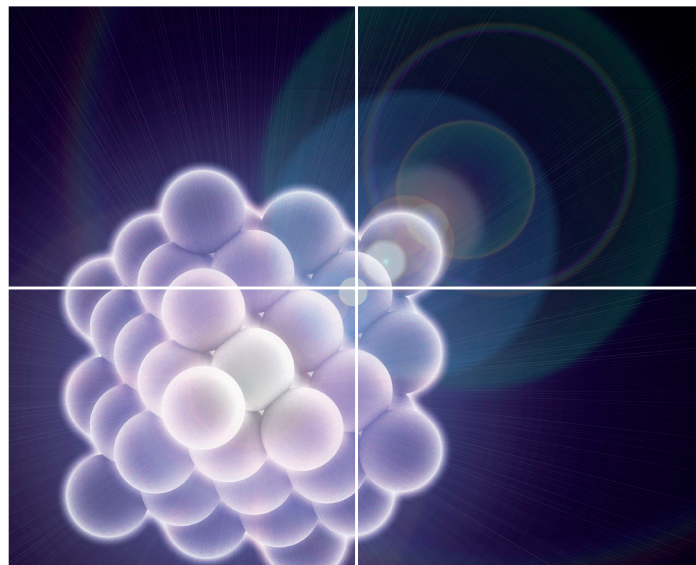


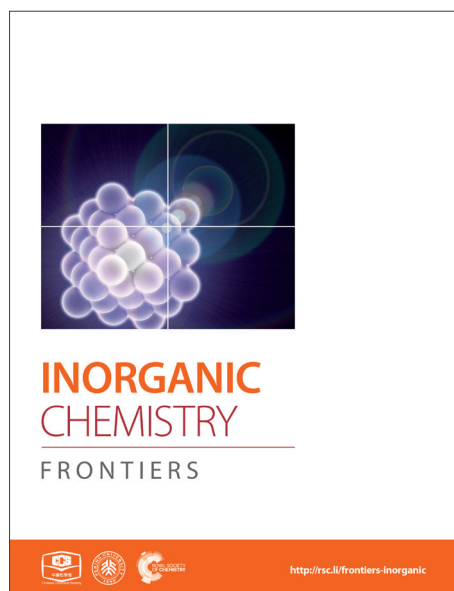
INORGANIC CHEMISTRY

FRONTIERS

Accepted Manuscript



This article can be cited before page numbers have been issued, to do this please use: X. Liu, W. Zhao, H. Cui, Y. Xie, Y. Wang, T. Xu and F. Q. Huang, *Inorg. Chem. Front.*, 2015, DOI: 10.1039/C4QI00163J.



This is an *Accepted Manuscript*, which has been through the Royal Society of Chemistry peer review process and has been accepted for publication.

Accepted Manuscripts are published online shortly after acceptance, before technical editing, formatting and proof reading. Using this free service, authors can make their results available to the community, in citable form, before we publish the edited article. We will replace this *Accepted Manuscript* with the edited and formatted *Advance Article* as soon as it is available.

You can find more information about *Accepted Manuscripts* in the [Information for Authors](#).

Please note that technical editing may introduce minor changes to the text and/or graphics, which may alter content. The journal's standard [Terms & Conditions](#) and the [Ethical guidelines](#) still apply. In no event shall the Royal Society of Chemistry be held responsible for any errors or omissions in this *Accepted Manuscript* or any consequences arising from the use of any information it contains.

ARTICLE

Organic-inorganic Halide Perovskite Based Solar Cells — Revolutionary Progress in Photovoltaics

Cite this: DOI: 10.1039/x0xx00000x

Xiangye Liu,¹ Wei Zhao,² Houlei Cui,² Yi'an Xie,² Yaoming Wang,^{2,*} Tao Xu,^{3,*} Fuqiang Huang^{1,*}Received 00th January 2012,
Accepted 00th January 2012

DOI: 10.1039/x0xx00000x

www.rsc.org/

The photovoltaic technology has been endowed with a huge chance, owing to the latest unprecedentedly rapid progress as a new-type solar cell based on organic-inorganic halide perovskite. The power conversion efficiency (η) has surpassed 19% since the first perovskite-based solar cell ($\eta=3.8\%$) was reported in 2009. Moreover, that performance seems to be still far from fully optimized because of its versatile fabrication techniques and device configurations. In this review, the history of perovskites for photovoltaic application and the landmark achievements to date were briefly outlined. Focusing on this new solar absorber of halide perovskites, crystal structure, electronic structure, and intrinsic physical properties are systematically described, attempting to unravel the origin of superior solar cell performance. From the requirements of high-efficiency photovoltaics, the unique solar perovskite absorbers and electron and hole transport materials are discussed, as well as some opening questions and challenges facing their further development and commercialization.

1. Introduction

Sunlight, the most abundant and clean renewable energy source, is definitely capable of the sustainable economic growth. Since the photovoltaic (PV) effect was discovered by Edmond Becquerel in 1839, researchers and engineers have been infatuated with the idea of developing efficient and cost-effective materials and PV cells to directly convert solar photons into electric power. Multicrystalline Si solar cells, known as the first generation PV cells, are currently dominant in the PV market with photoelectric conversion efficiency (PCE) close to 20% (for 1 cm² cells). However, the high production cost lays them an inextricable limit in large-scale civil application. The second generation PV cells based on thin film devices achieved a relatively significant progress in the aspect of diminishing manufacturing cost. Among various thin-film semiconductor compounds, copper indium gallium diselenide (CIGS) has been the star material for its high PCE (21.7 % for 0.5 cm² cells), comparable to mono-crystalline Si, but a remarkable lower cost, less efficiency-decay under long-time irradiation and excellent weak light performance. While the widely used vacuum manufacturing techniques made it not achieving full success in large-scale production.

In the last decade, the “new concept type” PV cells based on nanotechnologies and inexpensive solution processes have seen great strides. Dye-sensitized solar cell (DSSC) is the front runner in this new PV technology due to its cost-effectiveness, ease of fabrication and high efficiency. Furthermore, DSSCs configuration relaxes the material quality requirements met in the Si solar cells, owing to the separate transport of photo-generated electrons and holes in different materials. Mesoscopic DSSC based on nanocrystalline TiO₂ sensitized by

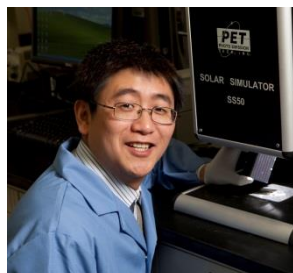
Ru(bpy)₃²⁺ was first introduced by Grätzel in 1985 and then a stirring PCE record of 12%¹ was achieved by his team in 1991 that spurred lots of scientific efforts into this type of devices. Recently, a PCE exceeding 13% was reported using Porphyrin photosensitizer and cobalt (II/III)-based redox electrolyte². However, organic sensitizers have inevitably been limited by their low light-harvesting ability and bad enduring stability. In order to replace conventional organic-type sensitizers, inorganic semiconductor quantum dots (QDs) were intensively investigated, such as metal-chalcogenides (CdS, PbS, Sb₂S₃, etc.), and III-V group semiconductors. Their numerous outstanding properties, including tunable energy band gaps, large optical absorption coefficients and carrier multiplication, unfortunately, have not endowed the PV cells with high performance. Significant losses of photo-generated carriers are mainly caused by the electronic trap states presented in the semiconductor nanocrystals owing to their high ratio of surface area to volume³.



Xiangye Liu is currently a 4th year PhD student in the College of Chemistry and Molecular Engineering, Peking University, under the guidance of Prof. Fuqiang Huang. He received his BS degree in chemistry from Hebei University, China in 2011. His thesis research focuses on design and synthesis of nanomaterials for solar energy applications.



Prof. Yaoming Wang received his PhD in chemistry from Shanghai Institute of Ceramics, Chinese Academy of Sciences in 2009. He became associate professor in Shanghai Institute of Ceramics, Chinese Academy of Sciences in 2012. He is an expert on CIGS and CdTe thin film solar cells. His current research interest is new Cu-based solar materials and new photovoltaic devices including perovskite-type solar cells.



Prof. Tao Xu received his PhD in Chemistry from The University of Alabama in 2003. He worked as a post-doc in Texas A&M University and Argonne National Laboratory during 2003-2006. He became an Assistant Professor at the Department of Chemistry and Biochemistry, Northern Illinois University in 2006 and was promoted to Associate Professor in 2011. His current research interest is nanoscale materials for energy and environmental science and applications.



Prof. Fuqiang Huang received his PhD in chemistry from Beijing Normal University in 1996. He worked as a research staff in University of Michigan, Northwest University, Osram Sylvania Inc. and University of Pennsylvania during 1996-2003. He became a Professor in Shanghai Institute of Ceramics, Chinese Academy of Sciences in 2004 and joined as a full professor in College of Chemistry and Molecular Engineering, Peking University in 2010. His current research interest is energy materials and photovoltaic applications.

Recently, the emergence and development of organic-inorganic halide perovskite-based solar cells (PSCs) have kindled tremendous researching enthusiasm, owing to their miraculous combining of high efficiency and low cost solution-based fabrication process. Since the first report of $\text{CH}_3\text{NH}_3\text{PbX}_3$ ($X = \text{Br}, \text{I}$) sensitized liquid junction cell in 2009⁴, the PCEs of the PSCs have rocketed to 19.3%⁵. That is a booming progress which is rarely seen in every other historical solution-processed solar cell technology. Therefore, the halide perovskite's excellent properties of light harvesting and charge transfer have undoubtedly opened a new era for the PV technology.

In this review, we will first describe the crystal structure and the intrinsic physical and electronic properties of this class of halide perovskites, attempting to unravel the origin of their superior solar cell performance. Then we will focus on the progress in PSCs, referring to the device configuration, working principles and fabrication technology, followed by the summary of the different perovskite materials, the electron transport materials (ETMs) and the hole transport materials (HTMs). Finally, we end up with a brief summary and outlook of the perovskite-based PV cells.

2. Intrinsic properties of halide perovskite

2.1 Crystal structure

Perovskite first refers to a kind of oxide mineral of calcium titanate, with the chemical formula of CaTiO_3 . This mineral is discovered in Ural Mountains of Russia by Gustav Rose in 1839 and is named after the Russian mineralogist Lev Perovskite⁶. Now the word of "perovskite" is chosen to describe any compound crystallized in the same structure as CaTiO_3 . A pure perovskite compound can be presented by the general chemical formula AMX_3 , where both A and M are cations and X is an anion. In an ideal perovskite structure, M is octahedrally coordinated with X forming a building block of MX_6 , and MX_6 octahedra connect with each other sharing every corner to be a three-dimensional network, shown in Figure 1. A cations fill in the hollows formed by every eight adjacent MX_6 octahedra and thus balance the charge of the entire network (Figure 1b). Large numbers of inorganic perovskite oxides and halides have been extensively studied owing to their versatile properties in optics⁷, magnetics⁸, electrics⁹ and electrochemistry¹⁰.

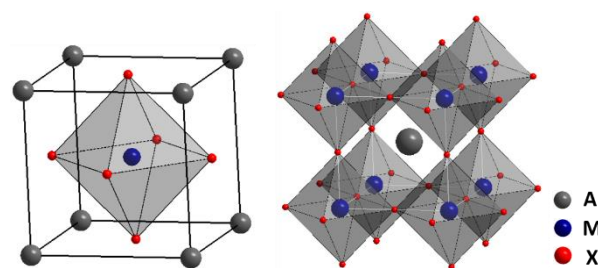


Figure 1. Crystal structure of cubic perovskite of general formula ABX_3 .

For the organic-inorganic halide perovskites discussed here, A cations are organic ammoniums, and M cations are divalent metal ions such as Cu^{2+} , Mn^{2+} , Pd^{2+} , Sn^{2+} , Eu^{2+} , etc., while the X anions are halides (Cl^- , Br^- , I^-). These belong to a large family which have attracted extensively scientific interests since 1970s for their structural versatility and magnetic, optical, and electric properties¹¹. The organic-inorganic halide perovskite systems with metal ions Sn^{2+} or Pb^{2+} in the M site generated the initial interests in the early 1990s, focusing on their semiconductor-metal transition property^{12, 13}, high carrier mobility for thin film transistors¹⁴ and strong excitonic feature for light-emitting diodes¹⁵. Not until 2009⁴ did the class of compounds MAMX_3 ($\text{MA} = \text{CH}_3\text{NH}_3$; $M = \text{Pb}, \text{Sn}$; $X = \text{Cl}^-, \text{Br}^-, \text{I}^-$) reignite scientific excitement as new visible-light absorbers and excellent charge transport materials for PV cells, which led to the renaissance of this organic-inorganic perovskite material. In these compounds, the $[\text{MX}_6]^{4-}$ octahedra can form chained¹⁶⁻¹⁸ or layered or three dimensional (3D) networks depending on the characteristics of organic ammonium cations at the A site.

A general formula for a typical $\langle 100 \rangle$ oriented layered organic-inorganic halide perovskites can be written as $(\text{R-NH}_3)_2\text{MA}_{n-1}\text{M}_n\text{X}_{3n+1}$, where R-NH_3^+ is alkylammonium or phenethylammonium^{11, 12}. The $\langle 100 \rangle$ oriented inorganic perovskite sheet alternates with bilayer of R-NH_3^+ organic cation and n refers to the number of the perovskite sheet. The NH_3^+ head of the organic cations are hydrogen/ionic bonding to the halogens in perovskite sheets and the hydrocarbon tails R extending into the space between the perovskite sheets forming

a van der Waals gap. As the $n \rightarrow \infty$, MAMX_3 with a 3D structure is encountered. That is shown in Figure 2.

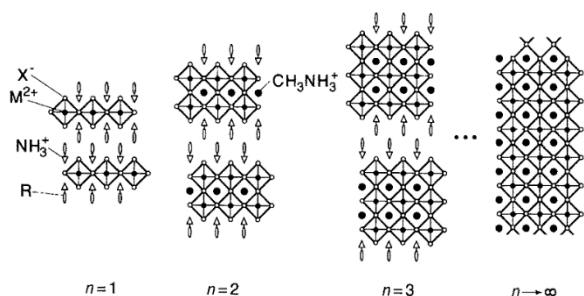


Figure 2. Schematic illustration of the $\langle 100 \rangle$ oriented hybrid perovskite family with the general formula of $(\text{R-NH}_3)_2\text{MA}_{n-1}\text{M}_n\text{X}_{3n+1}$. (Reproduced with permission¹¹)

As with the 3D perovskites AMX_3 , their crystallographic structure formability can be empirically estimated by the Goldschmidt tolerance factor t and an octahedral factor μ . $t = (t_A + t_X)/[2^{1/2}(t_M + t_X)]$ and $\mu = t_M/t_X$, where t_A , t_M , and t_X are the effective ionic radii for the ion at the A, B, and X sites, respectively. A study of the formability of alkali metal halide perovskites proposed that the ideal cubic structure was stabilized provided the t factor ranges between 0.813 and 1.107 and the μ factor ranges from 0.442 to 0.895¹⁹. Lower t value gives a lower symmetric tetragonal or orthorhombic structure. Taking MAPbX_3 for example, the radii of $\text{MA}^+ = 180$ pm, $\text{Pb}^{2+} = 119$ pm, $\text{Cl}^- = 181$ pm, $\text{Br}^- = 196$ pm, and $\text{I}^- = 220$ pm, thus the t factors for MAPbX_3 are calculated at 0.85, 0.84, and 0.83, and the μ factors are 0.66, 0.61, and 0.54, for $X = \text{Cl}$, Br , and I ,

respectively. Thus, methylammonium lead halide perovskites are expected to have a cubic structure. Despite these constraints, phase transitions of MAPbX_3 occur with the variation of temperature. The temperature-dependent structures of MAPbX_3 are summarized in the Table 1. At low temperature, MAPbX_3 formed in an orthorhombic phase (space group: $Pnma$), which successively transforms into tetragonal (space group: $I4/m$) and cubic structure (space group: $Pm\bar{3}m$) with the increase of temperature. The position of the MA^+ can only be fixed in the orthorhombic phase at low temperature, because it is characterized disordered in the higher symmetric structures. For example, a cubic structure requires eight identical positions for the cation in such a way that the tetrahedral coordinated C and N atoms show random distribution inside the eight tetrahedrons of the cuboctahedron around the normal A position $(1/2, 1/2, 1/2)^{20}$. A more recent work studied the structure of MAPbI_3 in detail with the variable temperature powder X-ray diffraction²¹. Results show that MAPbI_3 has a tetragonal structure at room temperature, which transforms to a cubic phase when heated to 57.3 °C and to an orthorhombic structure when cooled down to about 100 K. From cubic to tetragonal to orthorhombic structures, there is a continuous tilting of the $[\text{PbI}_6]$ octahedra around the c axes^{20, 21}. It is worth to note that the structure of perovskite is not simply depended on temperature. For example, high energy X-ray diffraction data showed that 70% of MAPbI_3 within mesoporous TiO_2 formed in a highly disordered phase with a structural coherence length of only ~ 1.4 nm, although MAPbI_3 film was annealed at 100 °C²². Fully characterizing and controlling the crystallinity of the perovskite layer is important for its improved photovoltaic performance.

Table 1. Temperature dependent structure data of MAPbX_3 . (Reproduced with permission²⁰)

Phase	Temperature	Crystal system	Space group	Lattice (pm)	Volume (10^6 pm ³)
MAPbCl₃					
α	> 178.8	cubic	$Pm\bar{3}m$	$a = 567.5$	182.8
β	172.9 – 178.8	tetragonal	$P4/mmm$	$a = 565.6$ $c = 563.0$	180.1
γ	< 172.9	orthorhombic	$P22_1$	$a = 567.3$ $b = 562.8$ $c = 1118.2$	357.0
MAPbBr₃					
α	> 236.9	cubic	$Pm\bar{3}m$	$a = 590.1(1)$	206.3 (260 K)
β	155.1 – 236.9	tetragonal	$P4/mcm$	$a = 832.2(2)$ $c = 1183.2(7)$	819.4
γ	146.9 – 155.1	tetragonal	$P4/mmm$	$a = 589.4(2)$ $c = 586.1(2)$	
δ	< 144.5	orthorhombic	$Pna2_1$	$a = 797.9(1)$ $b = 858.0(2)$ $c = 1184.9(2)$	811.1
MAPbI₃					
α	> 327.4	cubic	$Pm\bar{3}m$	$a = 632.85(4)$	253.5
β	162.2 – 327.4	tetragonal	$P4/mcm$	$a = 885.5(6)$ $c = 1265.9(8)$	992.6
γ	< 162.2	orthorhombic	$Pna2_1$	$a = 886.1(2)$ $b = 858.1(2)$ $c = 1262.0(3)$	959.5

2.2 Electronic structure

Earlier research work has calculated the Pb and Sn based halide perovskites (3D and low-dimensional) using the formalism of the extended Hückel theory as well as an *ab initio* Hartree-Fock LCAO approach²³. The calculation result overestimated the band gap energy of MAPbX_3 . The first principles density functional theory (DFT) band calculations on the room temperature cubic phase MAPbX_3 reveal that its

electronic structure is dominated by the characteristics of the Pb-X bonds^{24, 25}. The top of valence band (VB) mainly consists of the σ -antibonding states of Pb 6s and X p orbitals, and the bottom of the conduction band (CB) is primarily composed of the σ -antibonding states of Pb 6p and X s orbitals. In spite of these hybridization states, Pb 6p orbitals and X p orbitals separately dominate the CB minimum (CBM) and VB maximum (VBM), because the electrons in Pb 6s form in lone-pair configuration that will not lose from their s orbital²⁶.

Recently, three phases of MAPbI₃ were calculated with DFT theory accompanied by the generalized gradient approximation (GGA)²¹. The calculated band structures of cubic, tetragonal, and orthorhombic phases are shown in Figure 3. The results show MAPbI₃ has a direct band gap of 1.3 eV at the R point (Figure 3a) for the cubic structure, 1.43 eV at the Γ point (Figure 3b) for the tetragonal structure and 1.61 eV at the Γ point (Figure 3c) for the orthorhombic structure. The band gap energy increases with the reduction of structure symmetry. The calculated band gap energy of the tetragonal phase is slightly smaller than the experimental value 1.5 eV²⁷ due to the well-known underestimation of DFT. DFT calculation with a using the non-local optB86b + vdWDF functional is found to be a suitable method to analyze the electronic property of MAPbI₃²⁸. The calculated band gap energy from this approach excellently agrees with the experimental data. The spin-orbit coupling (SOC) effect was taken into consideration within the calculation works of Jacky Even *et al.*²⁹ and Paolo Umari *et al.*³⁰. Due to SOC, the six energy levels at the CBM of MAPbX₃ (X = Br, I) undergo a dramatic splitting, leading to a notable band gap reduction (Figure 3d).

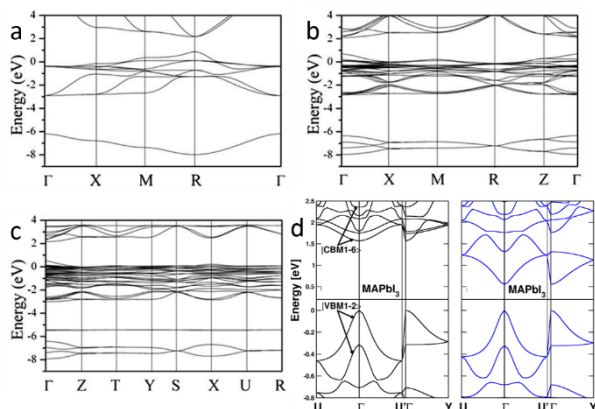


Figure 3. Electronic band structures of (a) cubic, (b) tetragonal, and (c) orthorhombic phases of MAPbI₃ along the high-symmetry lines in the first Brillouin (reproduced with permission²¹). (d) Comparison of electronic band structures of MAPbI₃ without (left) and with (right) the spin-orbit coupling interaction (reproduced with permission²⁹).

2.3 Unique charge separation and transport properties

Light-harvesting property. A high optical absorption coefficient is undoubtedly crucial for materials' PV application. A pure MAPbI₃ layer possesses a linear absorption coefficient of $5.7 \times 10^4 \text{ cm}^{-1}$ at 600 nm wavelength of light³¹, which is one order of magnitude higher than that of the N719 dye²⁷. The optical absorption coefficient of MAPbI₃ is also higher than that of conventional inorganic PV materials as GaAs, CdTe, and CIGS, evidenced by a calculation result (Figure 4a)²⁶. According to Wan-Jian Yin *et al.*'s work²⁶, the higher optical absorption coefficient of MAPbI₃ originate from its direct band gap *p-p* transition feature. Because the CBM and VBM of MAPbI₃ are mainly composed by Pb 6*p* orbitals and I 5*p* orbitals (which has been discussed above), the *p-p* transition is thus possible, which is generally much stronger than the *p-s* transition seen in CIGS, GaAs and so on. The *p*-orbital characterized CB minimum of MAPbI₃ has significantly higher density of states (DOS) than the *s*-orbital characterized CB minimums of GaAs, CdTe, CZTSe and CIGS (Figure 4b). That leads to a remarkable difference in the joint density of states (JDOS) (Figure 4c) which determines the optical absorption difference of these materials²⁶. A higher optical

absorption directly leads to a higher efficiency of the solar cell with a comparatively thinner absorber layer (Figure 4d), which will provide a shorter photo generated carrier pathway and consequently leads to a lower recombination rate.

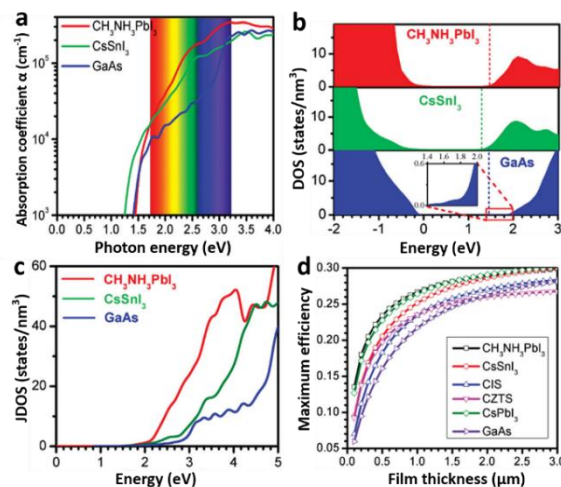


Figure 4. (a) The optical absorptions, (b) DOS and (c) JDOS of MAPbI₃, CsSnI₃ and GaAs. (d) Calculated maximum efficiencies of MAPbI₃, CIS, CZTS, and GaAs as a function of film thickness. (Adapted with permission²⁶)

Charge-transport property. In addition to those excellent light harvesting properties, MAPbI₃ is also characterized by efficient ambipolar electron and hole transport property. Due to this, comparatively higher efficiencies are achieved even in the PV devices without mesoporous *n*-type semiconductor³² or HTM³³, which is impossible for the N719 dye based solar cell. The outstanding charge transport properties of perovskites can be clearly seen from their ultra-long balanced electron-hole diffusion length. Femtosecond transient optical spectroscopy has concretely evidenced that the electron-hole diffusion length of solution processed MAPbI₃ is balanced to at least 100 nm, which is extremely long to be comparable to the optical absorption length³¹. For MAPbI_{3-x}Cl_x, the length value even surpasses 1 μm ³⁴. Long electron-hole diffusion lengths mean more electrons and holes can reach perovskite cell electrodes and create an external electrical current. The ultra-long electron-hole diffusion lengths might be the core advantage of organic-inorganic halide perovskites. It is worth to note that photo-excitation of the perovskite leads to the generation of electron-hole pairs which exist as free carriers or excitons, and the thermal equilibrium of those species is eventually reached in the perovskite absorber. Presently, it is still unclear what charge carriers are dominantly attributed to the perovskite's exceptional properties of long diffusion lengths. However, exciton in MAPbI₃ belongs to Wannier-Mott type for its long Bohr radii (22 Å). Its binding energy is calculated to be ~50 meV according to the high frequency limit ($\epsilon_\infty \approx 6.5$) at low temperature³⁵. At room temperature, the effective dielectric constant of MAPbI₃ is notably increased because of the rotational motion of CH₃NH₃⁺ cations, which leads to a significant enhanced screening effect of the Coulomb interaction between the electrons and holes. This screening effect further lowers the exciton binding energy to ca. 15 to 5 meV which is even smaller than $k_B T$ ~26 meV (k_B is the Boltzmann constant and *T* is the temperature) at room temperature. Thus the excitons are completely screened by the collective orientational motion of the organic cations, yielding almost free carriers at room temperature³⁶. This is totally different from the dyes usually used in DSSC, which feature the formation of

tightly bound excitons. Furthermore, excitons with such low binding energy in MAPbI₃ are easy to be efficiently split at the interfaces in PV devices.

The electron–hole diffusion length of a material is directly determined by its mobility and lifetime of the charge carriers. On the one hand, the effective masses of photo-generated electrons and holes in MAPbI₃ estimated by spin-polarized DFT calculations are $m_e^* = 0.23m_0$ and $m_h^* = 0.29m_0$, respectively³⁷. These values are comparable with that of silicon ($m_e^* = 0.26m_0$, $m_h^* = 0.29m_0$)²⁶, and the hole effective mass is much smaller than that of CuInSe₂ ($m_h^* = 0.75m_0$)²⁶, CuInS₂ ($m_h^* = 1.3m_0$)³⁸ and comparable with that of Cu₂ZnSnSe₄ ($m_h^* = 0.26m_0$)²⁶, GaAs ($m_h^* = 0.34m_0$)²⁶ and CdTe ($m_h^* = 0.28m_0$)^{26,39}. That small hole effective mass of MAPbI₃ can be deduced from its large dispersion of the VBM (Figure 3), which is extremely enhanced by the antibonding coupling effect between Pb lone-pair 6s² orbitals and I 5p orbitals²⁶. The small effective masses of photo-generated carriers lead to a high mobility (over 11 cm² V⁻¹s⁻¹)³⁷. On the other hand, extremely low charge carrier recombination rate of perovskite has been characterized by Snaith using transient THz spectroscopy, which reflects a long lifetime of their charge carriers⁴⁰. Furthermore, benign grain boundaries as evidenced by first-principle calculations, also accounts for their long charge carrier lifetime. Calculation results show that all the defects that create deep levels have high formation energies, while defects with low formation energies all have transition energies less than 0.05 eV above (below) VBM (CBM), forming shallow levels⁴¹. In addition, grain boundaries (GBs) in the polycrystalline MAPbI₃ layer do not generate any deep states in its band gap, resembling to the above shallow effects²⁶.

Though we have got some distinct hints physically by calculations, why organic-inorganic halide perovskites have such long electron–hole diffusion lengths remains mysterious. The unique structural properties of organic-inorganic halide perovskite might be the reason. The size of the organic cation is able to induce stress or confinement effects that can then determine the optoelectronic properties of the material itself. Then, how these unique structural properties affect the way of charges separation and transport, and why these unique structural properties will endow the materials with exceptional excellent photoelectric properties remain open questions.

Huang *et al* have proposed a simple model based on the crystal packing factor (PF) to evaluate the charge separation/transport abilities and photoelectric related properties of the materials with similar composition or structure^{42–44}. This simple model may shed some light on the reason for exceptional excellent photoelectric properties of the organic-inorganic halide perovskite. The concept came from Prof. John B. Goodenough's idea that lower elastic stiffness can promote distortion, which increases internal field, and can be easily implemented using the PF^{45,46}. Lower PF structure with lower elastic stiffness possesses higher internal electric field, resulting in more efficient charge separation/transport and thus better photoelectric related properties.

In terms of carrier diffusion length, which is associated with the carrier lifetime and mobility, PF model can provide good explanations on the better properties for looser structure. An open structure (lower PF value) provides free space for atom vibrations, leading to a higher momentary polarizing field. The more polarizable structure results in larger exciton Bohr radius, hence longer carrier lifetime. In addition, a lower PF structure is usually more deformable, which lowers the hopping barrier for polarons, thus increasing their mobility. The combination of increased carrier lifetime and mobility causes the higher charge separation/transport abilities. Some famous photoelectric materials have very low PF

values. Anatase TiO₂ with excellent photocatalytic effect has a PF of 0.65^{47–49}; BiFeO₃^{50,51}, Bi₂FeCrO₆ (whose PCE has reached 8.1% very recently)⁵² and KBiFe₂O₅⁵³ with excellent ferric photovoltaic effect have PFs of 0.66, 0.61 and 0.56, respectively. As for the organic-inorganic halide perovskites, we treat CH₃NH₃⁺ as one atomic ion for simplicity. The PFs of MAPbCl₃, MAPbBr₃, and MAPbI₃ are deduced to be 0.58, 0.61 and 0.65 respectively, and this is extremely low as compared to the value of over 0.7 for most inorganic perovskites. If considering the internal spatial openness of CH₃NH₃⁺, the PF should be even lower. The extreme structure-openness of organic-inorganic halide perovskites enables large micro-deformation and/or spatial vibration in local structure, which endows efficient electron-hole separation and charge transport, *i.e.*, long charge carrier diffusion length.

Photo-ferroelectric property. Additionally, carrier separation and transport in MAPbI₃ based PV cells can be enhanced by an possible ferroelectric effect due to the electric dipole of the MA⁺ cation (*i.e.* [CH₃]^{δ+}–[NH₃]^{δ–})⁵⁴ and the distortion of the [PbI₆]^{4–} network. MA⁺ cations are disordered located and rotates with high rates at room temperature⁵⁵. When an external electric field is applied, a transition from para- to ferroelectric molecular dipole order associated with the re-orientation of [PbI₆]^{4–} network will occur in MAPbI₃. Additionally, a novel photo-ferroelectric effect exists here⁵⁴. On the one hand, light excitation can facilitate the free rotation of MA⁺ cations by decreasing their binding energy to the [PbI₆]^{4–} cages⁵⁶; on the other hand, photoinduced carriers dramatically enhance the polarizability of the perovskite structure through intense electron–phonon coupling⁵⁷. Indeed, ferroelectric material as a light absorbing layer has been employed in PV devices, in which the voltage output along the polarization direction can be significantly larger than the bandgap of the ferroelectric materials⁵⁸. The hysteresis of halide perovskite has been observed in resistivity measurements⁵⁹. The presence of ferroelectric domains in high-quality β-MAPbI₃ thin films has been confirmed by the piezoforce microscopy (PFM)⁶⁰. Calculated results showed the presence of ferroelectric domains would result in internal junctions that may facilitate separation of photoexcited electron-hole pairs, and the reduction of recombination through segregation of charge carriers⁵⁵. Further experimental support is expected.

3. Progress in the organometal halide perovskite based solar cells

So far plenty of research works have sprung up with the focus on the PSCs. Despite of the versatility of device architectures and constituent materials, PSCs are mainly composed by the following function units: transparent front electrode (usually the FTO or ITO or AZO on glass or on flexible polymer substrate), the perovskite light-absorber, two or one of the two auxiliary charge transfer units, *i.e.*, the ETM (with or without mesoporous structure) and the HTM, and the counter electrode that has proper work function (>5.0 eV), including Au or Ag, Ni as well as carbon materials^{61–63}. Next, we will discuss in detail about the perovskite-based PV device architectures, dynamic mechanisms, fabrication techniques and the materials of the perovskites, ETMs and HTMs. Finally, we end this section with some measurement problems of the PSC performance.

3.1 Progress in the device architecture and the landmark efficiencies

3.1.1 Perovskite sensitized liquid mesoscopic cells

The organometal halide perovskites were initially present in the sensitized solar cell architecture, as the substitution of traditional

organic dye molecules. The general configuration and working principle of the DSSC device are schematically illustrated in Figure 5a-b. Typically, DSSCs consist of a sandwich structure with a liquid electrolyte (mainly I^-/I_3^- redox couple in organic solvent) clipped between the Pt counter electrode and dye-sensitized mesoporous TiO_2 photoanode. Upon photo-excitation, the dye molecule injects electrons into the conduction band of TiO_2 and holes in the dye molecules are regenerated by electrons from the I^-/I_3^- redox in electrolyte. The electrons and holes respectively diffuse to the front and back contact, where they generate an electric current. The open circuit photovoltage corresponds to the difference in the quasi-Fermi level of the *n*- and *p*-type conductor under illumination. In 2009, Miyasaka and his coworkers⁴ reported the first perovskite sensitized solar cells utilizing $MAPbI_3$ or $MAPbBr_3$ as light absorbers replacing of the organic dye molecules, also on a TiO_2 mesoporous layers with the same halide liquid electrolytes. A significant efficiency of 3.81% was obtained from $MAPbI_3$ with photocurrent onset extended to 800 nm. An impressive photovoltage close to 1 V was obtained from $MAPbBr_3$, associated with its higher conduction

band compared to that of the iodide. The electron injection from $MAPbX_3$ ($X = Br, I$) into TiO_2 with hole reduced by the redox couple is considered to be possible, according to the corresponding energy levels, as shown in Figure 5c. Latterly, Park *et al.*⁶⁴ fabricated the same type cells using 2-3 nm perovskite quantum dots sensitized on a 3.6 μm -thick TiO_2 mesoporous film iodide redox shuttle. The solar cell efficiency was improved to 6.5% with maximum external quantum efficiency (EQE) of 78.6% at 530 nm. Perovskite quantum dots exhibited better light absorption than the conventional N719 dye sensitizers, but they dissolved gradually in the electrolyte, resulting in a rapid degradation of performance.

Therefore, replacing the problematic liquid electrolytes with a solid-state HTM, *i.e.* fabricating all-solid solar cells, becomes an effectively way to stabilize the perovskites with respect of enhancement in PV performance.

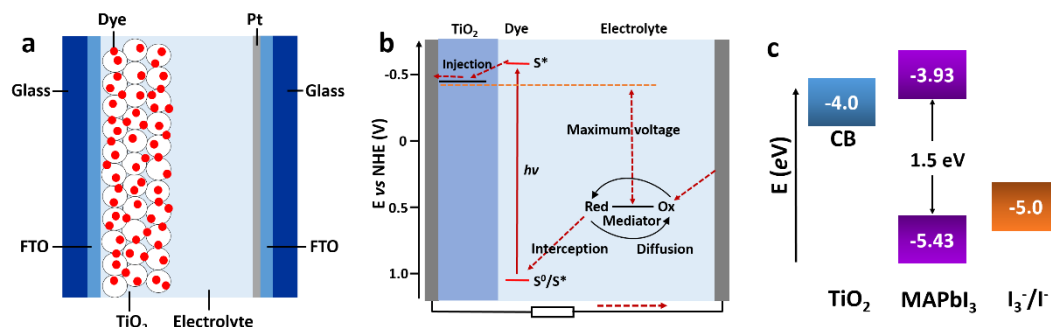


Figure 5. Schematic illustration of the general configuration (a) and working principle (b) of a DSSC (adapted with permission⁶⁵). (c) The energy level diagram of TiO_2 , $MAPbI_3$, and the redox couple of I_3^-/I^- (adapted with permission^{4,27}).

3.1.2 Perovskite sensitized solid-state mesoscopic cells

Grätzel, Park and colleagues²⁷ firstly introduced the spiro-MeOTAD (2,2',7,7'-tetrakis(N,N-di-p-methoxyphenylamine)-9,9'-spirobifluorene) solid HTM which has been applied in the solid-state DSSC in 1998⁶⁶. Then the PSC evolves into a solid-state mesoscopic configuration²⁷, where the $MAPbI_3$ nanoparticles were deposited onto the mesoscopic TiO_2 film, followed by the coating of the spiro-MeOTAD layer, and a 60 nm-thick Au layer serves as the back electrode. The pores of mesoscopic TiO_2 film are infiltrated with the spiro-MeOTAD. The cross-sectional structure of the device is shown in Figure 6a. The schematic band alignment is shown in Figure 6b, where the band positions are well aligned for charge separation. This device achieved a breakthrough PCE of 9.7% ($J_{sc} = 17.6 \text{ mA cm}^{-2}$, $V_{oc} = 888 \text{ mV}$ and $FF = 0.62$), with respectable long term stability that the overall PCE remained largely unchanged up to 500 h, even the devices were stored in air without encapsulation. After that, a jump to a PCE of 12.0% was demonstrated by Grätzel, Seok and coworkers⁶⁷, with the same structure cell but replacing the spiro-MeOTAD by poly-triarylamine as the HTM. By the new-type HTM, an obviously higher V_{oc} (997 mV) was obtained. The PCE was then improved to 12.4% by using a pyrene arylamine HTM and further improved to 15% by adopting a sequential deposition route.

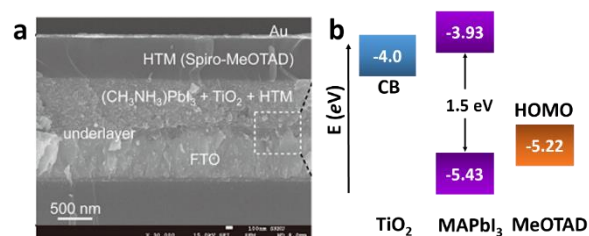


Figure 6. (a) Cross-sectional SEM image of the perovskite-based solid-state mesoscopic solar cell with spiro-MeOTAD as the HTM. (b) The energy level diagram of TiO_2 , $MAPbI_3$, and the spiro-MeOTAD. (Adapted with permission²⁷)

3.1.3 Solid-state planar heterojunction cells

In 2012, Snaith and co-workers³² utilized mesoporous Al_2O_3 instead of TiO_2 with the mixed halide $MAPbI_{3-x}Cl_x$ and spiro-MeOTAD. A relatively high PCE of 10.9% was obtained with a distinctively high V_{oc} of 0.98 V, which is identified to be ascribed to the absence of chemical capacitance in the TiO_2 . The insulated mesoporous Al_2O_3 serves only as the scaffold for the perovskite particles, other than an electron acceptor, because the electron injection is impossible due to the higher VBM of Al_2O_3 than that of the perovskite, as shown in Figure 7a. Therefore, the electrons must remain in the perovskite phase and transport through the perovskite film until they are collected by the compact TiO_2 coated FTO electrode. Concerning the mesoscopic structure but the absence of the electro-injection nature found in DSSC, this device was termed as "meso-superstructured solar cell" (MSSC)³².

This work revealed an unimaginable fact that perovskite did not form isolate quantum dots to serve as sensitizers, instead, it formed a continuous film to effectively transport photo-generated carriers. The success of the MSSC solar cells has driven explorations into planar thin film heterojunction PSCs, leaving out the preparation of the mesoporous *n*-type semiconductors.

The initial trial of planar thin film solar cell has been performed in Snaith's work³², but with a relatively low efficiency of 1.8%. The difficulties to make planar cell may step from the challenge of the deposition of homogeneous pin-hole free perovskite layer with high surface coverage, because the crystalline perovskite likely to dewet or agglomerate upon annealing. With optimized film formation of the mixed halide $\text{MAPbI}_{3-x}\text{Cl}_x$, by controlling the atmosphere, annealing temperature, and film thickness, Snaith and his co-workers⁶⁸ obtained a high PCE of 11.4%, with outstanding J_{sc} of 20.3 17.6 mA cm^{-2} and V_{oc} of 0.89 V. The typical configuration of planar thin film cell is shown in Figure 7b. The continuous perovskite film is directly contacted with the compact TiO_2 layer and the HTM layer. Yang and co-workers⁶⁹ reported a PCE of 12.1% with a low-temperature vapor-assisted solution process. Great success was achieved by Snaith's⁷⁰ group with an ultrahigh PCE of 15.4%, J_{sc} of 21.5 mA cm^{-2} and V_{oc} of 1.07 V, utilizing a vapor-deposition process. This result strongly confirmed that perovskite can be functioned in a simplified high efficient device, without the need of any complex nanostructure. After that, the PCE of perovskite planar heterojunction solar cell was improved to 15.7% by Kelly and his colleague⁷¹, and boosted to 19.3% lately contributed by Yang's group⁵.

After the miraculous ambipolar transport property of $\text{MAPbI}_{3-x}\text{Cl}_x$ with electron-hole diffusion length exceeding 1 μm is experimentally confirmed³⁴, a hole conductor-free planar thin film cell becomes possible, in which efficient hole-transporting is just along the perovskite layer. Indeed, with a simple heterojunction of $\text{MAPbI}_3/\text{TiO}_2$ (Figure 7c), Etgar and his colleague⁷² achieved a PCE of 8%, with a high J_{sc} of 18.8 mA cm^{-2} , but relatively low V_{oc} of 0.712 V. Very recently, Grätzel group⁷³ reported a printable hole-conductor-free cell with a double layer of mesoporous TiO_2 and ZrO_2 as a scaffold infiltrated with perovskite. A special mixed-cation perovskite $(5\text{-AVA})_x(\text{MA})_{1-x}\text{PbI}_3$ was utilized with lower defect concentration and better pore filling as well as more complete contact with the TiO_2 scaffold. The cell achieved a PCE of 12.8% with a higher V_{oc} of 0.858V, and was stable for >1000 hours in ambient air under full sunlight.

PSCs could also be constructed in an inverted structure where the ETM is connected with the metal electrode and the HTM is deposited on the conductive glass, shown as Figure 7d. The device with such structure commonly has an organic ETM (e.g. fullerene or its derivatives as [6,6]-phenyl C61-butyric acid methyl ester (PCBM) or indene- C_{60} bisadduct (ICBA)) and the HTM of poly (3,4-ethylenedioxythiophene) poly (styrenesulphonate) (PEDOT:PSS). A high efficiency of 12% was achieved with a device structure ITO/PEDOT:PSS/PolyTPD/ MAPbI_3 /PCBM/Au where perovskite layer was sandwiched between two organic charge-transport layers. Proper energy levels of each layer promised effective charge transfer and collection, yielding a high performance device⁷⁴. The PCE of device with the same structure is improved to 14.1% after improved a LiF interlayer⁷⁵. By using organic charge transport layer, flexible devices could be fabricated and a relatively high PCE of 9.2% has been achieved⁷⁶.

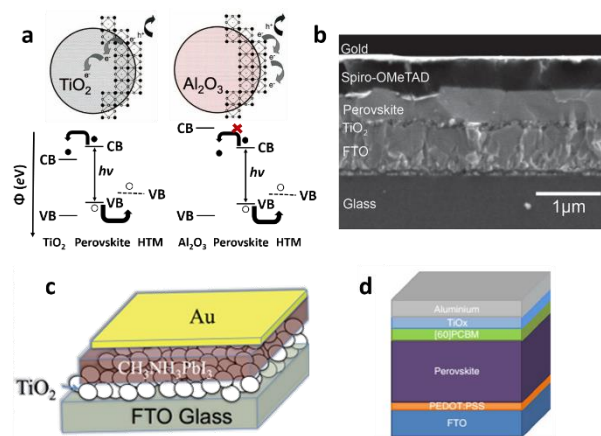


Figure 7. (a) Schematic illustration of the charge separation transport in a perovskite-sensitized TiO_2 solar cell and a noninjecting Al_2O_3 -based one (reproduced with permission³²). (b) Cross-sectional SEM image of a typical perovskite-based solid-state planar heterojunction solar cell (reproduced with permission⁶⁸). Schematic illustration of a perovskite-based planar heterojunction PV device (c) without HTM layer and (d) with a inverted structure (reproduced with permission^{72, 77}).

3.2 Progress in dynamics and mechanisms

Despite of the rapid progress in performance of the PSCs, the understanding of the dynamics and underlying mechanisms of such devices has not proceeded at the same pace. As described above, successes have been achieved in various configurations of PSCs, such as perovskite on mesoporous *n*-type semiconductor, perovskite on mesoporous insulator, and the perovskite-based planar thin film solar cells. Open questions thus exist on a series of topics: (i) Are there significant differences among the working principles of the various configuration devices? (ii) What are the factors that significantly affect the device performance? Focusing on these questions, many efforts are underway to analyze the two primary successive steps in the various PV devices, i.e. accumulation of photogenerated charge and charge separation. Elucidating those mechanisms is of fundamental importance for understanding the working principle of each type of PV devices, and for their further optimization.

The planar configuration device is expected to work in the following principle: the photo-generated excitons and free carriers co-exist in the perovskite layer and effectively transport along here due to the ambipolar charge transport property of the perovskite. Electrons and holes are separately collected by the ETM and HTM layers. Recently, mechanism of the planar configuration PSC has been directly probed by direct measurement of electron beam-induced current (EBIC) profiles of the device⁷⁸. The EBIC profile is useful for pinpointing the location of a driving force for charge separation, which is especially suited for determining the working principle of a photovoltaic device. In this technique, multiple electron-hole pairs are generated by the high-energy electron beam (as high energy photons do in the case of so-called multiple exciton generation). The EBIC signal is a current derived from the charge separation if there is any possible driving force.

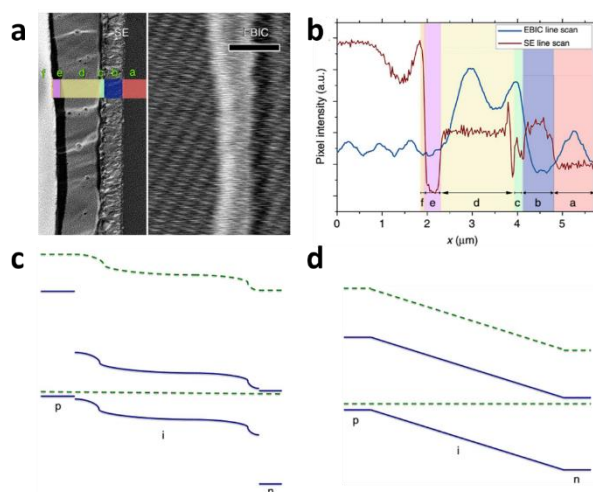


Figure 8. (a) Second electron (SE) image (left) and EBIC image (right) of the cross-section of the HTM/MAPbI_{3-x}Cl_x/compact TiO₂ solar cell. Letters designate the different layers of the device: f, Au; e, HTM; d, MAPbI_{3-x}Cl_x; c, TiO₂; b, FTO; a, glass. (b) SE and EBIC line scans at the indicated regions. A schematic diagram of band energy in the (c) MAPbI_{3-x}Cl_x-based solar cell with a separated hetero-junction configuration and in the (d) 'a-Si:H'-like based solar cell with a homogeneous built-in electric field. (Adapted with permission⁷⁸)

The typical line scan of the HTM/MAPbI_{3-x}Cl_x/compact TiO₂ solar cell is shown in Figure 8b. It is featured by two distinct peaks respectively near the interface of HTM/MAPbI_{3-x}Cl_x and that of MAPbI_{3-x}Cl_x/compact TiO₂, indicating the existence of two distinct built-in fields which are respectively associating with hole-extraction and electron-extraction. The decrease of the EBIC signal to the middle of the perovskite film results from any possible recombination during the carrier diffusion across the perovskite film to their preferred contact. These results provide direct experimental evidence of the *p-i-n* mode of operation of a perovskite-based planar thin film solar cell. Furthermore, this *p-i-n* mode is composed by two separate hetero-junctions with higher electron-extraction efficiency than that of hole-extraction, seen from the different intensities of the two EBIC signal peaks. In consideration of the energy levels of the relevant material bands, a schematic band diagram of the cell can be illustrated as Figure 8c, which is distinct from the homogenous built-in electric field ('a-Si:H'-like) (Figure 8d). Separate hetero-junction configuration contributes to minimize the dark current and maximize the photocurrent, and by their mutual contribution lead to an increased V_{oc} .

EBIC signals with the same two-peak feature were observed in the cells employing insulated mesoporous oxide (cell configuration: HTM/MAPbI_{3-x}Cl_x on mesoporous Al₂O₃/compact TiO₂), indicating that this kind of devices operate also as a *p-i-n* mode⁷⁸. However, in the absence of HTM, little field at the perovskite/Au junction was found and the active junction was then between the perovskite and the TiO₂⁷⁸. That explains the comparatively lower V_{oc} of the solar cell without HTM.

When tackling with the work principle of the PV devices with perovskite on mesoporous n-type semiconductor, *e.g.* TiO₂, controversies are encountered: (i) whether a sensitized or a heterojunction solar cell, *i.e.*, whether electrons are injected from the perovskite into mesoporous TiO₂, or just effectively transported through the perovskite itself; (ii) if the two pathways co-exist, which is more efficient and what is the ratio of them?

Moser, Grätzel and collaborators⁷⁹ has presented clear evidence of efficient electron injection from photoexcited MAPbI₃ into TiO₂, as

well as the evidence for efficient hole injection from photoexcited MAPbI₃ into HTM. In this work, Femtosecond pump-probe transient absorption experiments were carried out for MAPbI₃ deposited on TiO₂ and Al₂O₃ films, with and without HTM. The infrared probe allowed direct observation of the carrier's population decay within the perovskite itself, results shown in Figure 9a. The larger amplitude for the slower part of the decay observed for the perovskite on TiO₂ compared to that of perovskite on Al₂O₃, indicated that some of the charges had already been separated through ultrafast electron injection in to TiO₂ CB. Likewise, the hole injection process was evidenced by the fact larger amplitude for the device with HTM than one without. Complementary evidence for electron injection from perovskite to TiO₂ was obtained by the time-resolved microwave photoconductance measurements.

In that work⁷⁹, authors unravelled the mechanism of the charge transfer processes in this kind of solar cells, illustrated as Figure 9b. The desirable processes are (i) electron injection to TiO₂ and (ii) hole injection to the HTM, which are the primary charge separation step followed by the transport of free electrons and holes respectively to their selective contacts. Undesirable processes include the exciton annihilation in perovskite itself — (iii) photoluminescence recombination and (iv) non-radiative recombination, and back charge transfer at three interfaces — (v) TiO₂/perovskite, (vi) HTM/perovskite, and (vii) TiO₂/perovskite (this may occur at the region where perovskite is absent). The kinetics of these processes is expected to determine the performance of the overall device. From the results of transient optical absorption spectroscopy in this work, timescales of the above processes in the TiO₂/perovskite/HTM configuration is estimated as follows: the processes of (i) and (ii) have comparable ultrafast timescale of femtosecond-to-picosecond; nanoseconds for the processes of (iii) and (iv), but they were extensively suppressed due to the large amount of longer-lived charges caused by the efficient charge separation at the two interfaces; microseconds for the processes of (v) to (vii). Therefore, charge recombination processes ((iii) to (vii)) occur on a much slower timescale than the charge separation and extraction processes ((i) and (ii)), leading to the high performance of the PV device.

Grätzel and collaborators⁷⁹ consider that the injection process is more efficient and preferable for higher device performance, thus charge recombination is shown to be significantly slower on TiO₂ than on Al₂O₃ films (Figure 9c), because electron injection is not thermodynamically feasible in Al₂O₃. However, the questions are still open here. Snaith and co-workers³² showed an opposite result that charge collection in MAPbI_{3-x}Cl_x/Al₂O₃ devices is faster than that in MAPbI_{3-x}Cl_x/TiO₂, by using transient photocurrent measurements. It indicates that the perovskite material itself is more efficient in transporting the negative charge than mesoporous TiO₂. Recently, controversies are more or less relaxed by the work of Cahen and co-workers⁸⁰. In this work, the EBIC measurement showed that holes are extracted significantly more efficiently than electrons in MAPbI₃, while the diffusion lengths of MAPbI_{3-x}Cl_x are comparable for both charge types. That explains why MAPbI₃-based cells require mesoporous electron conductors, while not does the MAPbI_{3-x}Cl_x-based ones. More interestingly, in MAPbI_{3-x}Cl_x-sensitized cell, the existence of two complementary paths for electron transport, involving either TiO₂ or MAPbI_{3-x}Cl_x was also suggested⁸¹. Zhu and co-workers^{82, 83} showed the almost overlapped curves (electron diffusion coefficient as a function of photoelectron density and recombination lifetime as a function of open-circuit voltage) for mesostructured MAPbI₃ and dye solar cells, indicating that the mechanistic factors governing the charge transport in the MAPbI₃/mesoporous-TiO₂ based solar cells are similar to those in the DSSCs. Therefore transport in the perovskite cells is dominated

by the electron conduction within the TiO_2 network rather than from the perovskite layer itself. These sensitized characters of PSCs were further confirmed by Snaith *et al.*⁸⁴ and Grätzel *et al.*⁸⁵ by means of impedance spectroscopy measurement. However, Bisquert *et al.*⁸⁶ found that the photo-generated charges were mainly accumulated in the MAPbI_3 layer for the $\text{MAPbI}_3/\text{mesoporous-TiO}_2$ based PV device from impedance spectroscopy. That is essentially distinct from the conventional DSSC where instantaneous injection from the dye into the TiO_2 occurs and no charge accumulation is observable in the light absorber. Additionally, their latter work⁸⁷ demonstrated that the dominant carrier transport pathway is the perovskite layer in the mesoscopic structured cell. Long carrier diffusion lengths (1 μm) are first measured by impedance spectra, in correspondence with the value of perovskite layer obtained from time-resolved photoluminescence³¹.

In a summary, the PSCs with planar configuration or with insulate oxide scaffold work in a *p-i-n* model or a *p-n* model (devices without HTM); working principle for perovskite/mesoporous *n*-type

semiconductor based solar cell is controversial, where the exact ratio of electrons injected into the mesoporous *n*-type semiconductor and that transported through the perovskite is unknown. Even so, the nanostructured scaffold at least has the following advantages: (i) it can provide large area for deposition of perovskite light-absorber; (ii) it can prolong the light-absorption length; (iii) the perovskite film deposited on it is relatively thin which can reduce the carrier transport length.

According to the work principles of the PSCs discussed above, the main factors that significantly affect the device's performance can be summarized here: the intrinsic material properties, such as band gap, the energy levels of the CB and VB or HOMO and LUMO, and the charge transport properties; the device parameters, such as layer thickness, homogeneity, surface coverage degree, morphology, crystalline quality, contact quality of different functional layers, the density of defect, and so on. So the performance of the PV device can be optimized by tuning the materials composition and improving the fabrication techniques.

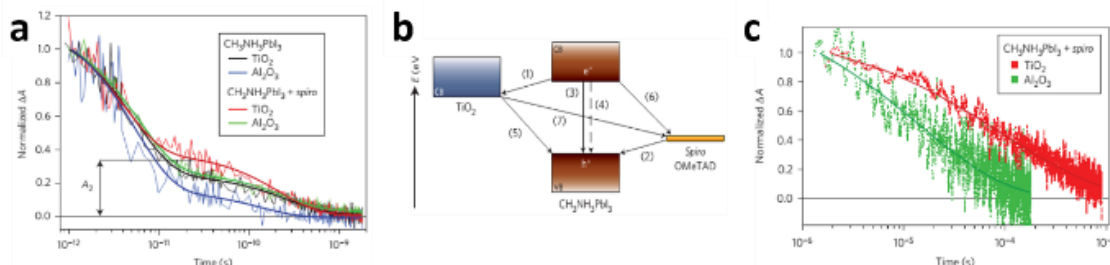


Figure 9. (a) Transient absorption signals of MAPbI_3 in various system measured at a probe wavelength of 1.4 μm following femtosecond laser pulsed excitation at 580 nm. Thick solid lines represent bi-exponential fits of experimental points starting at $t = 1$ ps. A_2 represents the normalized absorbance change at 25 ps, used as a metric to compare the various samples. (b) Schematic illustration of energy levels and charge transfer processes in the perovskite-sensitized solid-state solar cell. (c) Charge recombination dynamics obtained from nanosecond laser flash photolysis in the HTM –present devices of $\text{MAPbI}_3/\text{TiO}_2$ (red) and $\text{MAPbI}_3/\text{Al}_2\text{O}_3$ (green). The recombination is apparently slower when TiO_2 is used than Al_2O_3 . Thick lines represent stretched exponential fit of data. (Reproduced with permission⁷⁹)

3.3 Progress in fabrication techniques

Generally, the fabrication of an entire PSC is based on the layer-by-layer process with the sequential deposition of ETM on the front electrode substrate, followed by the deposition of perovskite and HTM layers, and completed by the deposition noble metal counter electrode with thermal evaporation method. Spin coating dominates the deposition process of the ETM and HTM, while hydrothermal *in situ* growth of TiO_2 or ZnO is also feasible. However, the fabrication technique of the perovskite layer is versatile and has the crucial effect on the device performance.

For the deposition of the perovskite layer, so far there have been four different methods: one-step solution deposition, two-step sequential solution deposition, vapor-assisted solution process and dual-source vapor deposition. The first one is the simplest method which is most commonly used. The last three methods possess special merits in optimizing the perovskite film in the aspect of crystallinity, morphology, and homogeneity. At the same time, solution-based methods to prepare perovskite nanoparticles⁸⁸⁻⁹⁰ have also been reported, which have potential application in the fabrication of PV devices.

3.3.1 One-step solution deposition

Firstly, the precursor solution of perovskite is prepared by dissolving the powder of RAX ($\text{RA} = \text{MA}^+$, or other alkyl ammonium cation; $\text{X} = \text{Br}, \text{I}$) and PbX_2 ($\text{X} = \text{Cl}, \text{Br}, \text{I}$) at a proper mole ratio (usually, at 1 : 1) in aprotic polar solvents (γ -butyrolactone (GBL), dimethyl formamide (DMF), dimethyl sulfoxide (DMSO), N-2-methyl pyrrolidone (NMP), *etc.*) to get a clear solution. Secondly,

the solution is spin-coated on the ready-prepared *n*-type contact layer. Finally, an annealing process at approximately 100 $^\circ\text{C}$ is needed to transform the precursor to crystalline perovskite. The depositing process has better to avoid moisture, preventing the decomposing of the perovskite. With this fabrication technique several parameters could be tuned to further optimize the device performance, such as the solvent and concentration of precursor solution, thickness of the perovskite layer, anneal temperature and time.

Snaith and co-workers⁶⁸ have studied the effects of anneal temperature and thickness on the morphology of the perovskite layer. Results show that as anneal temperature increases, the number of pores in the final film decreases, while the surface coverage of perovskite is also reduced due to the agglomeration process which results in perovskite islands. With increasing initial film thickness, the average pore size increases, while the surface coverage also increases. The optimized condition is considered to be the anneal temperature of 90 $^\circ\text{C}$ and the initial perovskite film thickness of 450–550 nm. With this condition, a uniform full-coverage perovskite film without any pin hole can be fabricated. On the one hand, it enables collection of a higher fraction of incident photon, which lead to higher J_{sc} ; On the other hand, the increased coverage removes a shunt path to avoid leakage currents, leading to higher FF and V_{oc} . In their later interesting work⁹¹, leveraging the dewetting of perovskite films to form microstructured arrays of “islands”, they fabricated neutral color semitransparent solar cells where islands are thick enough to absorb all visible light, whereas the void space are visibly transparent. The preparation atmosphere, precursor solvent and the film anneal temperature are well controlled in their work. Grätzel’s group⁹² also studied the anneal temperature effects on the perovskite

film with a precursor solution of PbCl_2 and MAI (1 : 3 molar ratio) in DMF. They found that complete conversion into desired perovskite phase requires a temperature at least 80 °C and sufficiently higher is required for the crystallization of the perovskite material. However, too high annealing temperature (above 140 °C) leads to the additional formation of PbI_2 , which will decrease the light absorption and hinder the injection of charges to and from the TiO_2 , leading to poor J_{sc} , V_{oc} and FF . Conings and co-workers⁹³ exploited DMSO as the solvent to prepare perovskite precursor of high concentration up to 60 wt%. With this precursor, they have yielded reasonably smooth perovskite films with up to >95% coverage and thicknesses exceeding 200 nm, thus enabling light absorption close to 100%, and resulting in very reproducibly higher efficiency values (especially higher J_{sc}) compared to the devices made from low-concentration precursors.

3.3.2 Two-step sequential solution deposition

Burschka and co-workers⁹⁴ firstly introduced the two-step sequential deposition method to fabricate perovskite sensitized mesoscopic solar cells. In this deposition procedure, the solution of PbI_2 in DMF was first spin-coated onto the nanocrystalline TiO_2 film and subsequently transformed into the perovskite by dipping into the solution of MAI in iso-propanol. It was found that the conversion occurs within the nanoporous TiO_2 host as soon as the two components come into contact, which was impossible if without the nanopores confinement. This confinement effect permits much better control over the perovskite morphology than is possible with the common one-step deposition method. Employing this technique into the fabrication of PV cells greatly improves the PCE (to a value of 15%), as well as the devices' reproducibility and stability. This finding opened new routes for the fabrication of PSCs with superior performance. Following this sequential deposition method, Grätzel's group⁹⁵ fabricated highly efficient devices with a mixed cation perovskite. Additionally, Kelly and his colleague made a planar heterojunction cell with ZnO in place of TiO_2 , also adopting the sequential deposition method to prepare the perovskite layer. An ultrahigh PCE value of 15.7% was achieved by their device⁷¹.

3.3.3 Dual-source vapor deposition

In 2013, Snaith's group⁷⁰ reported the dual-source vapor deposition technique to prepare the perovskite film for the planar heterojunction solar cell. In their process, MAI and PbCl_2 were used respectively as the organic and inorganic precursor, evaporated simultaneously from separate sources in vacuum condition with proper molar ratio, on to a rotated ready-prepared substrate (Figure 10). A dark reddish-brown film was observed immediately after evaporation, followed by an annealing process in N_2 atmosphere to crystallize the perovskite absorber layer. This deposition technique resulted in large scale extremely uniform and nanocrystalline perovskite films without any voids between the perovskite crystals, which is rarely in the solution-processed films. It thus avoided the possible direct contact between the compact TiO_2 and the HTM layer, a shunting path that is responsible for the lower FF and V_{oc} in the solution-cast planar PV devices. With this deposition method, a landmark PCE of 15.4% was obtained. After that, Nazeeruddin, Bolink and colleagues⁹⁶ employed this dual-source vapor deposition technique in the fabrication of PSC with organic ETM, achieving outstanding performance.

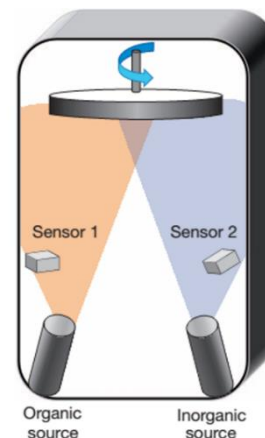


Figure 10. Schematic diagram of Dual-source thermal evaporation method for depositing the perovskite absorbers (reproduced with permission⁷⁰).

3.3.4 Vapor-assisted solution process

The vapor-assisted solution process can be viewed as a modified two-step sequential sequential solution deposition whose second step is replaced by a vapor deposition process. Yang and co-workers⁶⁹ invented this novel method to prepare MAPbI_3 film. In this process, the solution of PbI_2 in DMF was firstly spin-coated on FTO/compact- TiO_2 substrate. After drying, that was annealed in MAI vapor at 150 °C in N_2 atmosphere for desired time. The authors believed that incorporating organic species into the as-deposited inorganic framework through vapor effectively avoids the high reaction rate of perovskite during co-deposition of precursors and concern about possible film deterioration when dipping an inorganic framework into an organic species solution. The perovskite layer made by this technique featured with full surface coverage, small surface roughness, and grain size up to microscale, and 100% precursor transformation completeness. With the high quality perovskite film derived from this deposition method, an impressive PCE of 12.1% was achieved in a planar architecture solar cell⁶⁹. In a recent work of Yang's group, with the vapor-assisted solution process, PbI_2 species were ingeniously controlled to be exist at the perovskite grain boundaries and the interface of perovskite/ TiO_2 , which is in favor to reduce the carrier recombination⁹⁷. Therefore, this deposition technique opens a simple, controllable, and versatile approach to the pursuit of high-quality perovskite film and the resulting high-performance PV devices.

3.4 Progress in the materials of perovskites, ETMs and HTMs

3.4.1 Progress in the composition of perovskites

Different A cation. Although A cations contribute nothing to the band structure of the perovskite, their size can notably affect the symmetry of the $[\text{MX}_6]^{+}$ octahedral network depending on the different values of the tolerance factor t and thus alters the band gap. For example, for the three different A cations of $\text{HN} = \text{CHNH}_3^{+}$ (FA^{+}), $\text{CH}_3\text{NH}_3^{+}$ (MA^{+}) and Cs^{+} , there is a symmetry lowering trend: $\text{FAPbI}_3 > \text{MAPbI}_3 > \text{CsPbI}_3$. That is because the Pb-I-Pb bridging angles are gradually deviating from the ideal linear conformation from FAPbI_3 to CsPbI_3 , resulting in more and more reduced orbital overlap of Pb-I. Thus a corresponding band gap widening trend is encountered: $\text{FAPbI}_3 < \text{MAPbI}_3 < \text{CsPbI}_3$ ⁹⁹. By the design of mixture $\text{FA}_{1-x}\text{MA}_x\text{PbI}_3$ will red shift compared to that of MAPbI_3 (Figure 11a), thus an enhanced solar-light harvesting property is expected.

Furthermore, $\text{MA}_x\text{FA}_{1-x}\text{PbI}_3$ exhibits superior carrier-collection efficiency than the single-cation analogues, due to its longer exciton lifetime⁹⁵. Although FA^+ -based perovskites have narrower band gaps, they suffer from their unstability compared to MA^+ -based ones. Very recently, by rational incorporation of MAPbBr_3 into FAPbI_3 , a stable and efficient mixed-perovskite light-harvesting layer can be obtained, which has improved the device PCE to 18%⁹⁸.

Different B metal cation. The band gap of AMl_3 differs distinctly with different M ions (*e.g.* Ge^{2+} , Sn^{2+} and Pb^{2+}), following the trend $E_{\text{of}} \text{AGeI}_3 < \text{ASnI}_3 < \text{APbI}_3$. That is consistent with the energy level trend of $\text{Ge } 4p < \text{Sn } 5p < \text{Pb } 6p$. Apparently, Sn based halide

perovskites seemingly are more suitable for PV application than the Pb based ones, in light of their smaller band gaps and non-toxicity. Indeed, Sn based perovskites exhibit larger extent absorption of visible light³⁰ (Figure 11b) and a large red-shift of the incident photon to current conversion efficiency (IPCE) curve edge⁹⁹ (Figure 11c). However, the efficiency was compromised by the poor Sn(II) stability^{30, 59}. Relativistic GW calculation shows the different MASnI_3 and MAPbI_3 electronic properties are dominantly due to relativistic effects. These effects stabilize the MAPbI_3 material towards oxidation, by inducing a deeper valence band edge and thus a wider band gap compared to MASnI_3 ³⁰.

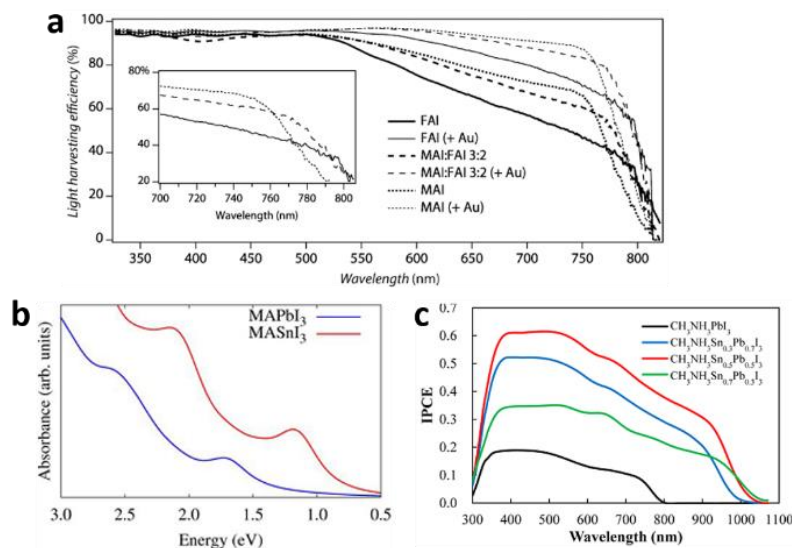


Figure 11. (a) Light-harvesting efficiency of $\text{MA}_x\text{FA}_{1-x}\text{PbI}_3$ (reproduced with permission⁹⁵). (b) Comparison between the relativistic GW calculated light absorption spectra of MASnI_3 and MAPbI_3 (reproduced with permission³⁰). (c) IPCE curves for $\text{MASn}_x\text{Pb}_{1-x}\text{I}_3$ based solar cells (reproduced with permission⁹⁹).

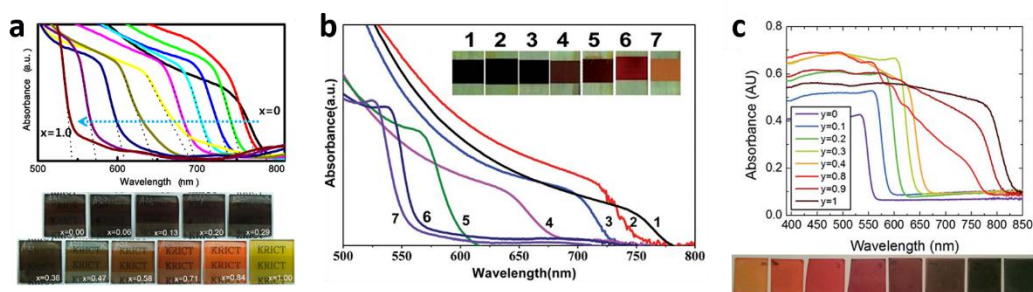


Figure 12. Photographs and UV-vis absorption spectra of $\text{MAPb(I}_{1-x}\text{Br}_x)_3$ films made by (a) one-step solution deposition and (b) two-step sequential deposition. (c) Photographs and UV-vis absorption spectra of $\text{FAPbI}_y\text{Br}_{3-y}$ films. (Reproduced with permission¹⁰⁰⁻¹⁰²)

Different X halide anion. Different halogen can significantly affect the band structure of MAPbX_3 (*e.g.*, the VBM sates, band gap). From Cl to Br to I, the band gap of MAPbX_3 is gradually decreased, resulting in a gradual red shift of the optical-absorption edge, which is due to that the VBM for MAPbX_3 are mainly dominant by X p orbital and minor hybridized states of lead with halide.^{21, 25} Their VBM states gradually upshift from Cl to Br to I. Mixed multi-halide anions in the perovskites allow for continuous tuning of the band gap and the optical absorption to cover almost the entire visible spectrum¹⁰⁰⁻¹⁰⁴ (Figure 12). It is worth to be mentioned

that the band gap of MAPbI_3 will increased after mixed with Br or Cl, resulting in a decreased absorption of visible light and a lower short-circuit current density (J_{sc}). However, a wider band gap can generate a higher open-circuit voltage (V_{oc}). That is the reason why $\text{MAPbBr}_{3-x}\text{Cl}_x$ based PV cells exhibit an ultrahigh V_{oc} (1.5 V), in spite of a relatively low J_{sc} (4 mA cm^{-2})¹⁰³. On the other hand, the incorporation of Cl into $\text{MAPb(I}_{1-x}\text{Cl}_x)_3$ is limited to a relatively low concentration levels (below 3–4%), owing to the large difference in the ionic radii of Cl^- and I^- and a low calculated formation energy^{25, 105}. More interestingly, nearly no band gap alteration after Cl mixed into MAPbI_3 which was evidenced both experimentally and calculatively^{32, 105}. In addition, compared to the single halide ion

perovskite, the mixed ones are more stable, as well as facilitating the charge transport^{32, 100, 105, 106}. The electron-hole diffusion length of

MAPbI₃³⁴. That is because MAPbI_{3-x}Cl_x ($\tau_e = 273 \pm 7$ ns) has a much longer recombination lifetime than that of MAPbI₃ (only $\tau_e = 9.6 \pm 0.3$ ns)³⁴. That fantastic diffusion length of MAPbI_{3-x}Cl_x makes thicker absorber layers becoming possible in order to harvest more light, and the nano or meso structures are no longer necessary.

3.4.2 Progress in ETMs

TiO₂ is the most common ETM employed as the blocking layer, or the nanostructured *n*-type scaffold for the perovskite. The TiO₂ blocking layer, *i.e.* the compact TiO₂ layer, is generally deposited by spin-coating technique using organic titanate solution. The compact TiO₂ layer is efficiently electron-selective and blocks the hole-collection in this electrode. For the nanostructured TiO₂ scaffold, continuous progress about the morphology and thickness study has been witnessed with the rapid development of the PSCs to accommodate the variety of device architectures.

Mesoporous TiO₂ scaffold deposited by doctor-blade method was initially introduced in the PSCs derived from the DSSCs. A well infiltration of the perovskite and the following HTM into the pores of the mesoscopic scaffold is preferable for high performance devices. In the PV devices of Kim *et al.*²⁷, increasing TiO₂ film thickness deteriorated the V_{oc} and FF, attributed to the increase of dark current and electron transport resistance according to the impedance spectroscopic study. While the photocurrent density was not strongly influenced by the thickness of TiO₂ layer from 0.6-1.4 μm , maintaining a high level of 16-17 mA/cm^2 due to the large optical absorption cross section. In the meantime, Etgar *et al.*¹⁰⁷ fabricated mesoscopic MAPbI₃/TiO₂ heterojunction solar cells based on anatase TiO₂ nanosheets exposing (001) facets with a side length of 30 nm and a thickness of 7 nm. The assembled simple MAPbI₃/TiO₂ cell shows a PCE of 5.5% under AM 1.5 solar light, which was relatively moderate due to the absence of hole conductor material.

Afterwards, Kim *et al.*¹⁰⁸ demonstrated the preparation of highly efficient PSC based on a submicrometer (0.6 μm) rutile TiO₂ nanorods. TiO₂ nanorods were grown on the FTO-coated dense TiO₂ layer substrates via hydrothermal synthesis method, and their length was adjusted by setting different reaction time. Then the MAPbI₃ and spiro-MeOTAD were spin-coated onto TiO₂ nanorod films subsequently. It was demonstrated that well-ordered 1D structure of shorter nanorod film was better for infiltration of spiro-MeOTAD than the longer nanorod film with disordered structure. Eventually, a PCE of 9.4% was achieved with about 0.6 μm -thick rutile TiO₂ nanorod film under one sun illumination, with a J_{sc} of 15.6 mA/cm^2 and a V_{oc} of 955 mV. Despite the significant reduction in surface area compared to nanoparticle films, the resultant J_{sc} exceeded 15 mA/cm^2 because of high absorption coefficient of perovskite MAPbI₃. When increasing the nanorod length, J_{sc} and V_{oc} decreased to varying degrees. The decrease in J_{sc} with increasing the nanorod length was likely to be related to either amount of the adsorbed perovskite or pore filling fraction, while the decrease in V_{oc} was related to the different charge generation as explained by impedance spectroscopy. Xu *et al.*¹⁰⁹ recently reported the rutile nanowire-based PSCs with highest efficiency of 11.7%. It was found that the best efficiency is achieved with 900 nm rutile single crystal nanowires, which provided a rapid electron transport pathway and subsequently led to the holes as the majority carrier in perovskite phase. J_{sc} in this case can reach 22 mA/cm^2 . They also used photovoltage rising transient to study the transport in presence of recombination, which provided insightful understanding on the compromise between the conflicting demands of light harvesting and charge transport.

the mixed halide (MAPbI_{3-x}Cl_x) is found to be greater than 1 μm , which is an order of magnitude greater than that of

In 2014, freestanding TiO₂ nanotube array films¹¹⁰ were first applied as electrodes in MAPbI₃-based solar cells, which were prepared by a two-step anodization process and then detached from the substrate by *in situ* field-assisted chemical dissolution and transferred onto FTO that was covered by a TiO₂ blocking layer. A sequential deposition approach was used to deposit the perovskite absorber into the nanotubes. MAPbI₃ sensitized nanotube based electrodes had significantly larger absorbance of visible light over the whole spectrum than nanoparticle based electrodes with the same thickness, ascribed to the enhanced light trapping ability of the nanotube arrays. Furthermore, charge recombination is effectively reduced in the nanotube based devices as indicated by photovoltage decay measurements. Therefore, the nanotube based cell yielded a higher PCE than nanoparticle based one, with an equal V_{oc} but a higher J_{sc} . The study of the dependence of photovoltaic performance on the nanotube film thickness showed that the photovoltaic performance increases with a decrease of the TiO₂ nanotube film thickness, due to the different photoexcited charge extraction and collection efficiencies. A preliminary photovoltaic performance with a photocurrent density of 17.9 mA/cm^2 and an efficiency of 6.52% was acquired from the cell with 2.3 μm TiO₂ nanotubes.

Although TiO₂ was commonly used as the electron transport layer and had appropriate energy levels for transferring electrons while blocking holes, its insufficient conductivity might lead to unnecessary ohmic losses or a nonideal space charge distribution within the cell. Photo-thermal deflection spectroscopy (PDS) measurements suggested that Al doping can reduce the number of sub-bandgap states of TiO₂ and dramatically increases its electron conductivity¹¹¹. PSCs using compact TiO₂ with Al-doping level of 0.3 mol% delivered an enhanced J_{sc} value, leading to an improved PCE of 13.8%, compared with a PCE of 11.1% for the undoped compact layer. Y doping is another way to improve the conductivity of TiO₂. Yang's group⁵ achieved a record PCE of 19.3% using Y-TiO₂ as the ETM. A higher conductivity (2×10^{-5} S/cm) for the Y-TiO₂ film versus the undoped TiO₂ film (6×10^{-6} S/cm) was obtained due to the increased carrier concentration and the series resistance in the device was also reduced from 9.12 to 5.34 ohms. The improved conductivity of Y-TiO₂ matched that of spiro-OMeTAD, 10-fold than that of pristine TiO₂, which balanced the carrier transport to reduce nonideal space charge distribution. Aforetime, Qin *et al.*¹¹² used mesoporous Y³⁺-substituted TiO₂ (0.5% Y-TiO₂) film to enhance the performance of PSCs. A PCE of 11.2% under simulated AM 1.5 full sun illumination was obtained, with a 15% improvement in J_{sc} compared with pure TiO₂. Graphene insertion to TiO₂ layer is also an effective way to assist electron transport and improved the photovoltaic performance^{31, 113}.

ZnO was considered to be a viable alternative to TiO₂ for PSCs due to its comparable energy levels as well as good electron transport properties. Kumar *et al.*¹¹⁴ reported ZnO-based PSC, which was the foremost demonstration of PSCs employing the ZnO compact layer as a hole blocking layer and a mesoscopic scaffold layer as an electron transporter. The ZnO compact layer was formed by electrodeposition and ZnO nanorods were grown by chemical bath deposition, completely processed at low temperature (<100 °C). The typical diameters of the ZnO nanorods grown on the ZnO film are in the range of 100-150 nm and the lengths were between 400-500 nm. The blocking-ZnO/ZnO nanorods based PSC exhibited a remarkable PCE of 8.90% with a high J_{sc} of 16.98 mA/cm^2 , while planar bi-ZnO based cell without nanorods demonstrated a smaller PCE of 5.54% and J_{sc} of 11.27 mA/cm^2 . The increment in the J_{sc} value for the nanorod morphology could be attributed to better charge generation and collection efficiency due to increased light

scattering and a larger heterojunction interface. Additionally, the mild conditions for fabrication of bl-ZnO/ZnO nanorods allowed the processing of flexible PSCs. A PCE of 2.62% was achieved from blocking-ZnO/ZnO nanorods based cell on flexible PET/ITO substrates.

Similarly, in 2014, Son *et al.*¹¹⁵ issued the 11% efficient PSC based on ZnO nanorods. They prepared ZnO seed layer by spin-coating and ZnO nanorods by solution process. Diameter and length of the hexagonal ZnO nanorods were manipulated by controlling concentration of the precursor solution and immersion time. After depositing MAPbI₃ absorber and spiro-MeOTAD HTM, the 82 nm wide and 1 μ m long ZnO nanorods based PSC demonstrated a J_{sc} of 20.08 mA/cm², V_{oc} of 991 mV, FF of 0.56 and PCE of 11.13%, which was so far the highest efficiency for the ZnO nanorods based dye-sensitized and PSCs. It was noteworthy that the results were acquired with the absence of a compact TiO₂ blocking layer, which should be substituted by the compact ZnO seed layer. By contrast, 1 μ m long TiO₂ nanorod film based cell was also prepared, resulting in J_{sc} = 20.92 mA/cm², V_{oc} = 869 mV, FF = 0.55 and PCE = 10.02%. The slightly higher PCE of ZnO nanorod was due to the higher V_{oc} associated with higher conduction band position for ZnO than rutile TiO₂ and slower recombination characteristics, indicating that ZnO nanorods were an effective charge collection system in PSCs. Liu *et al.*⁷¹ reported a planar PSC using low temperature processed ZnO nanoparticles as the blocking layer. And an impressive efficiency of 15.7% on FTO and 10.2% on flexible ITO substrates were achieved. The high performance of these cells is considered to be originated from the unconstrained MAPbI₃ perovskite crystallite growth that occurs in the absence of a mesoporous scaffold.

Fullerene (C₆₀) or its derivative is another selectable ETM which has been widely used in organic or inorganic-organic hybrid solar cells. Chen *et al.*¹¹⁶ presents a hybrid organic solar cell (OSC) that uses a planar heterojunction of MAPbI₃ perovskite/fullerene structure as the active layer, with a thin bathocuproine (BCP) film as a hole-blocking layer, achieving the optimized PCE of 3.0%. After applying PCBM or ICBA instead of C₆₀, the PCEs can be optimized to 3.9% and 3.4%, respectively. These results verify the formation of a donor-acceptor interface at the MAPbI₃/C₆₀ heterojunction and the modulation of photovoltaic performance by acceptors of varied LUMO levels. Snaith *et al.*⁸⁴ used the self-assembled monolayer C₆₀ functionalized mesoporous TiO₂ as the "mesoporous electron acceptor" for MAPbI_{3-x}Cl_x based solar cell, and a PCE of 6.7% was achieved. The C₆₀ monolayer acts as an electron acceptor but inhibits further electron transfer into the TiO₂ mesostructure, allowing a reduction of energy loss. This strategy opens an exciting and versatile route for hybrid PV devices. Perovskite/PCBM based flexible solar cell with a polymer substrate is reported by Snaith's group⁷⁷, obtaining a PCE of 6%. Similar configuration devices are fabricated by Bolink *et al.*⁹⁶, the PCE was improved to 7%. These results demonstrate the versatility of the perovskite thin-film technology to the broad variety of possible device configurations.

3.4.3 Progress in HTM

HTMs play a vital role in determining the photovoltaic performance of the PSCs, especially responsible for the high V_{oc} ¹¹⁷. Spiro-OMeTAD is most commonly used and extensively studied. However, its poor hole conductivity, high cost (complex synthesis process) and instability in ambient atmosphere (doping by nitrogen or oxygen) restrict its practical applications. Novel HTMs with outstanding performance and high stability are pursued and both inorganic and organic alternatives are explored during the last three years.

Organic HTMs. Both small molecules and conducting polymers have been studied as novel substituent HTMs and comparable

photovoltaic performance with spiro-OMeTAD was achieved. Several functional polymers such as P3HT, PCDTBT and PTAA were introduced as electron blocking layers, among which PTAA performed best with a maximum PCE of 12.0%⁶⁷. Jeon *et al.*¹¹⁸ also used PTAA as the HTM layer and achieved a certified PCE of 16.2%. P3HT, as a popular p-type conducting polymer was usually used as an active layer in OPVs, attracted great attention as a candidate. Abrusci⁸⁴ and Heo⁶⁷ almost reported simultaneously P3HT as the HTM layer, and efficiencies of 3.8% and 6.7% could be achieved. The photovoltaic performance of P3HT based solar cell could be further increased (from 9.2% to 12.4%)¹¹⁹ after doping P3HT with Li-TDSI and D-TBP. By sandwiching a hybrid perovskite film between selective contacts of TiO₂ and P3HT layers, Conings⁹³ and Giacomo¹²⁰ also fabricated PSCs with efficiencies close to 10%. A comparative study of different HTMs, including Spiro, P3HT, and DEH, was conducted to investigate the varied process of charge transport and charge recombination¹²¹. Hole transfer from perovskite to HTM under work condition was demonstrated by photoinduced absorption spectroscopy. The difference in electron lifetime was revealed to explain the different device performance. The authors also suggested design route to find new HTMs by controlling the perovskite/HTM interface together with matching energy levels.

Small molecules were also investigated as the HTM in PSCs. Spiro-OMeTAD doped with Li salt (LiTFSI) already showed impressive performance as HTMs although long-term stability should be resolved¹²². Modification of Spiro-OMeTAD was realized by using spiro(TFSI)₂ (a dicationic salt of spiro-OMeTAD) to increase the hole conductivity and operating stability¹²³. PSCs fabricated with spiro(TFSI)₂ gave a PCE of 10% comparable to that of conventional spiro-OMeTAD¹²³. Considering the cost and stability issue of spiro-OMeTAD, the development of novel small molecules based HTMs is imperative. Pristine tetrathiafulvalene derivative (TTF-1) without p-type dopants has suitable HOMO and LUMO positions with respect to the energy levels of perovskite was demonstrated by CV measurements¹²⁴. PSC using TTF-1 as the HTM layer achieved a PCE of 11%, which was comparable to that of p-type doping spiro-OMeTAD (11.4%)¹²⁵. Efficiency degradation comparison between TTF-1 and Spiro-OMeTAD indicated that pristine TTF-1 performed better under ambient conditions with the humidity of 40% and showed only 20% efficiency decrease after 500 h test. The enhanced durability was ascribed to avoiding the use of sensitive additives and the hydrophobic effect of alkyl chains. Except TTF-1, PSCs fabricated with thiophene, quinolizino acridine and phenylamine derivatives as HTMs also exhibited impressive photovoltaic performance¹²⁶⁻¹²⁸.

Inorganic HTMs. To date, the organic HTMs used in PSCs often suffered from high cost and low hole mobility. Exploring low cost and effective inorganic HTMs has attracted extensive attention. CuI was first demonstrated as an inorganic HTM in PSC and a PCE of 6% was achieved¹²⁹. CuI, as the HTM layer, rendered the PV devices with higher FF compared with spiro-OMeTAD because of higher electrical conductivity. CuI based device also exhibited better photocurrent stability than spiro-OMeTAD although the reason was unclear. However, the high charge recombination in CuI layer limited the V_{oc} . The solution to this problem could make CuI as a competitive replacement for spiro-OMeTAD¹²⁹. Another copper based p-type semiconductor CuSCN can also be employed as the HTM layer because of its good transparency, high hole mobility and good chemical stability. PCEs of 3.8% and 6.4% were respectively obtained by Sarkar's group¹³⁰ and Zaera's group¹³¹ using CuSCN as HTM. After optimization of perovskite layer morphology, a record PCE of 12.4% was achieved based on HTM of CuSCN¹³². Another important p-type oxide NiO could also be used as hole transport

layer in PSCs, often in an inverted structure. With the thin NiO nanocrystalline film as the HTM layer, a PCE of 9.11% has been achieved by Yang' group¹³³. If mesoscopic NiO as hole collecting electrode, a remarkable PCE of 9.51% was achieved¹³⁴. Electrodeposited NiO was also investigated as hole conductor in planar inverted PSC and a maximum PCE of 7.3% was obtained¹³⁰. UV-treatment was able to deepen the work function of NiO, which led to a higher V_{oc} of 1.05 V of the PSC¹³⁵. In addition, graphene oxide was also employed as a hole conductor in inverted PSC and gave a PCE over 12%¹³⁶.

3.5 Measurement problems of PSC performance

Hysteresis in current-voltage (J - V) curves of PSC is arising scientific attention, owing to its blockage for the measurement of steady-state power output, *i.e.* the real efficiency of the PSC. Hysteresis always manifests as the mismatch of the J - V curves scanned in the forward (from short-circuit to open-circuit) and reverse (from open-circuit to short-circuit) directions. It is also observed in other typical PV devices like DSSCs¹³⁷, CIGS, CdTe and amorphous silicon based solar cells^{138, 139}, and its origin is considered to lie in the chemical capacitance which can be charged up under forward scan (FS) and discharged under reverse scan (RS), resulting in a reduced external FS-photocurrent and increased RS-photocurrent¹⁴⁰. In those typical PV devices, hysteresis can be effectively suppressed by lower the scan rate. However, hysteresis in the PSC is anomalous that it gets more extreme as the scan rate is reduced, and even exists when at a very slow scan rate (e.g. 0.011 V/s)¹⁴⁰. The steady state power output can be obtained only by a stepwise J - V measurement with a delay timescale of many seconds, shown in Figure 13¹⁴¹⁻¹⁴³.

Snath *et al.*¹⁴⁰ initially suggested three possible origins for the hysteresis in the PSC: 1) Defects in perovskite or interface states which can act as traps for electrons and holes; 2) The ferroelectric properties of the perovskite; 3) The migration of excess ions. However, when considering the unusually long transient time in stepwise J - V curves (Figure 13), the possible origins of 1) and 3) seem to be not satisfactory. Moreover, the possibility of the interfacial-trap origin is impossible for the fact that the planar thin film PSC exhibits larger hysteresis than mesoporous TiO_2 based one whose interfacial traps are supposed to be more significant¹⁴¹. So the most possible origin of the hysteresis associated with the transient effects is the ferroelectric properties of the perovskite itself. The underestimated efficiency derived from FS-curve results from the excess polarization (with an opposite direction of built-in electric field) and relatively small dielectric constant of the perovskite at the initial stage. And the overestimated efficiency derived from RS-curve results from the opposite effect¹⁴³.

The ferroelectric polarization of the perovskite originates from the rotation of the MA^+ and the distortions of the inorganic framework which are able to align themselves with the external electric field. The dielectric relaxation of such a structure is demonstrated to be an extremely slow process, especially for the realignment of the inorganic framework⁵⁶. That explains the long-time scale of the transient effect (Figure 13) which is consistent with the capacitance and the characteristic time obtained at the low frequency in the impedance spectra (IS)^{57, 144, 145}. The slow dielectric relaxation process can also explain the anomalous hysteresis that does not appear in the case of very fast scan, because the realignment of the perovskite cannot follow the higher scan velocity. Thus with the decrease of the scan velocity, the hysteresis becomes remarkable, unless enough slow scan (e.g. $\ll 0.01$ V/s) to thoroughly eliminate the hysteresis¹⁴³. The ferroelectric properties of the perovskite could be significantly restrained by reduced crystal size because small grain size could reduce the number of ferroelectric domain wall.

That explains why mesoporous TiO_2 based PSC exhibits less pronounced hysteresis than planar thin film PSC, owing to the small size confinement by mesoporous TiO_2 ^{143, 146}. Moreover, the TiO_2 layer is able to release the polarization effect in perovskite through electron-injection, thus consequently to reduce the hysteresis. The capacitance at low frequency in IS decreases with the increase of thickness of TiO_2 layer¹⁴². The polarization property of perovskite is also depend on the growth condition and the type of organic cations and halide ions¹⁴⁴.

Additionally, light and voltage bias conditions prior to measurement can also have significant impact upon the shape of the measured J - V curves and the apparent device efficiency. It has been demonstrated^{141, 146} that pre-condition of light-soaking at forward bias is able to improve the FF and the photocurrent of the PSCs, leading to an apparently higher efficiency. And it can also reduce the hysteretic effect in J - V curves. Those effects can also be explained by the ferroelectric polarization of the perovskite, although some scientists attributed these effects to ion migration¹⁴¹. Illumination can dramatically increase the dielectric constant of perovskite and decrease the energy barrier for the polarization alignment in the perovskite^{56, 57}. Forward bias can generate an internal polarization filed which points to the same direction with the photocurrent. Consequently, pre-condition of illumination + forward bias effectively facilitate charge separation and transport, leading to superior device performance. On the contrary, dark-soaking or reverse bias lead to the opposite effects on the performance of PSCs^{141, 146}.

According to the analysis above, the measured J - V curves associated with the apparent efficiency of the PSC are hugely affected by various factors, such as the device structure, crystal size of perovskite, selective contacts, measurement details, and the pre-conditions. However, the real efficiency should be only obtained from the steady-state measurements regardless of any prior "history" of the device¹⁴⁰.

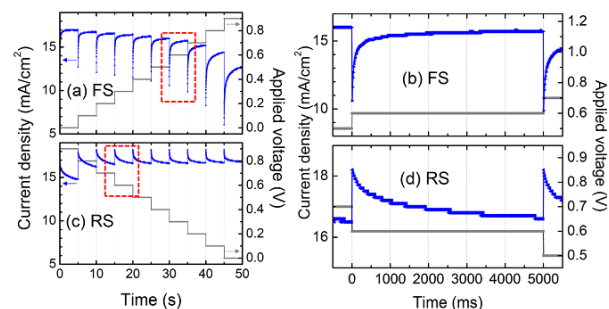


Figure 13. Photocurrent profile depending on time at (a) forward scan (FS) and (c) reverse scan (RS) at stepwise voltage sweep between 0 and 0.9 V. Time-dependent current response at the applied voltage of 0.6 V (shown in dashed-red rectangles) at (b) FS and (d) RS. Reproduced with permission¹⁴².

4. Summary and outlook

The organic-inorganic hybrid PSCs are undergoing an evolutionary progress for the photovoltaics. The PCE of this kind of solar cell soared faster than any other competing solar technology in recent years¹⁴⁷ (Figure 14), as well as the advantages of low cost and fabrication versatility. The powerful light-harvesting ability and excellent charge separation and transport capability of the perovskite could spark the design for next generation high performance PV devices. However, uncertainties till exist in the understanding of the working principles and the charge carrier dynamics of such devices, which may be the underlying breakthrough point for further eruption of their PV performance.

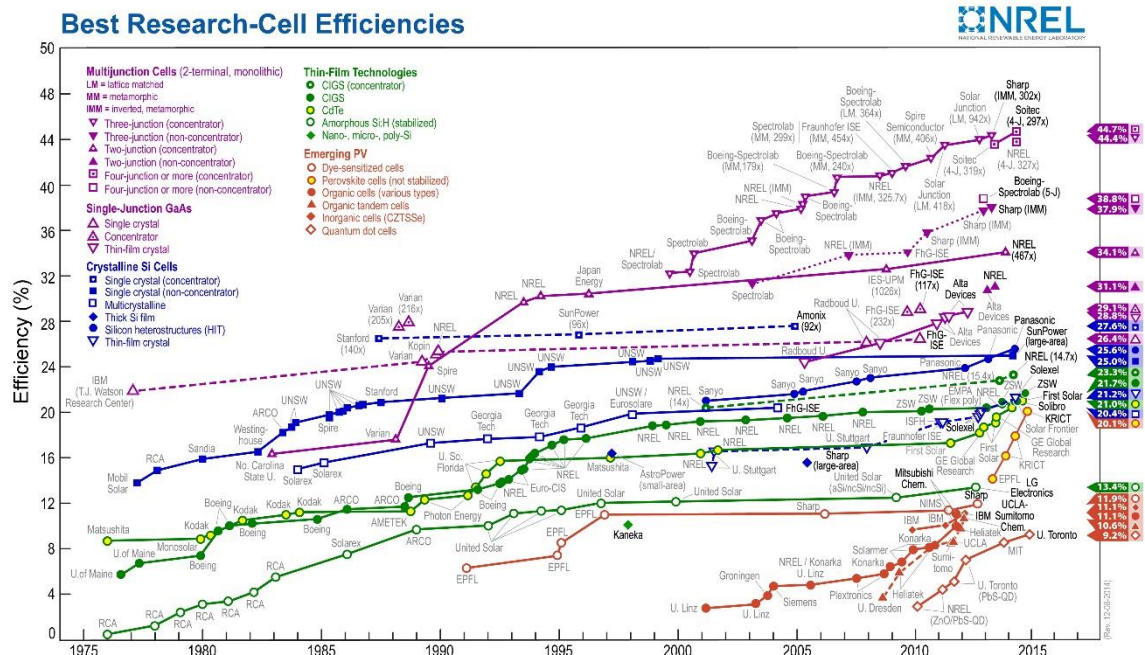


Figure 14. The rapid efficiency improvement of the PSCs compared to other PV technologies, data provided by the National Renewable Energy Laboratory (NREL). (reproduced with permission¹⁴⁸)

Hybrid tandem-junction solar cells are more attractive due to their improved overall PCE. Because of the success of PSC with an inverted structure, tandem-junction type of device is now possible by matching the perovskite-based system with other thin-film technologies of silicon, CIS, CIGS, CZTSSe¹⁴⁹, as shown in Figure 15.

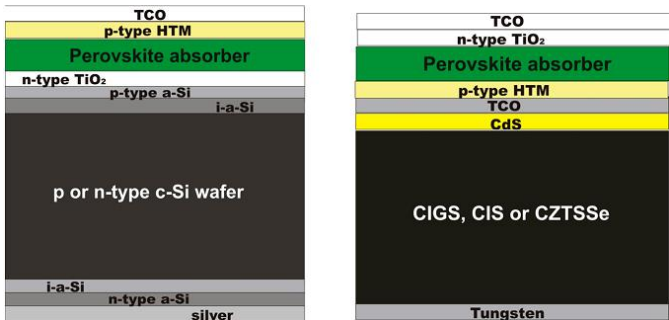


Figure 15. Schematic illustrations of the conceptual hybrid tandem-junction PV devices (reproduced with permission¹⁴⁹).

The major impediment of the presently studied perovskite lies in its instability and the toxicity of Pb. The organic-inorganic hybrid halide perovskite is susceptible to moisture, solution process, temperature and UV light radiation, which can greatly affect the composition and structure of the perovskite layer, thus detrimental to the charge separation and transport of the PV device¹⁵⁰. That resulted in more difficulties in the fabrication of the perovskite layer. Replacing Pb by Sn could be a possible way to eliminate the disadvantage of toxicity. Some remarkable progresses have been

seen in the Sn based PSCs, while their performances are still large-gap behind of that of Pb-based ones, and the instability of Sn-based perovskite is the main challenge^{99, 151}. So scalable technologies for industrial manufacture have to stress on the stability and toxicity. One more important question is whether these current perovskites are the best solar absorber materials and whether ones will develop other than perovskite-type absorbers with much better performances.

Overall, we believe it is promising to see the on-going efficiency improvements and the understanding of the material properties in the next few years, and the emergence of commercialized perovskite-based PV products might be on the horizon.

Acknowledgements

This work was financially supported from NSF of China (Grant nos. 61376056, 51125006, 91122034, 61204072), and Science and Technology Commission of Shanghai (Grant no. 13JC1405700, 14520722000).

Notes and references

- Beijing National Laboratory for Molecular Sciences and State Key Laboratory of Rare Earth Materials Chemistry and Applications, College of Chemistry, Peking University, Beijing 100871, P.R. China;
- CAS Key Laboratory of Materials for Energy Conversion, Shanghai Institute of Ceramics, Chinese Academy of Sciences, Shanghai 200050, P.R. China;
- Department of Chemistry and Biochemistry, Northern Illinois University, DeKalb, Illinois 60115, USA.

* Corresponding authors: Yaoming Wang (wangyaoming@mail.sic.ac.cn), Tao Xu (txu@niu.edu) and Fuqiang Huang (huangfq@pku.edu.cn); Fax: (+86)10-62758225.

- B. O'regan and M. Grätzel, *nature*, 1991, **353**, 737-740.
- A. Yella, H. W. Lee, H. N. Tsao, C. Yi, A. K. Chandiran, M. K. Nazeeruddin, E. W. Diau, C. Y. Yeh, S. M. Zakeeruddin and M. Gratzel, *Science*, 2011, **334**, 629-634.
- A. H. Ip, S. M. Thon, S. Hoogland, O. Voznyy, D. Zhitomirsky, R. Debnath, L. Levina, L. R. Rollny, G. H. Carey and A. Fischer, *Nature nanotechnology*, 2012, **7**, 577-582.
- A. Kojima, K. Teshima, Y. Shirai and T. Miyasaka, *J Am Chem Soc*, 2009, **131**, 6050-6051.
- H. Zhou, Q. Chen, G. Li, S. Luo, T.-b. Song, H.-S. Duan, Z. Hong, J. You, Y. Liu and Y. Yang, *Science*, 2014, **345**, 542-546.
- P. Gao, M. Grätzel and M. K. Nazeeruddin, *Energy & Environmental Science*, 2014, **7**, 2448.
- U. Schwarz, F. Wagner, K. Syassen and H. Hillebrecht, *Physical Review B*, 1996, **53**, 12545.
- R. von Helmolt, J. Wecker, B. Holzapfel, L. Schultz and K. Samwer, *Phys Rev Lett*, 1993, **71**, 2331.
- J. Haeni, P. Irvin, W. Chang, R. Uecker, P. Reiche, Y. Li, S. Choudhury, W. Tian, M. Hawley and B. Craigo, *Nature*, 2004, **430**, 758-761.
- J. Suntivich, H. A. Gasteiger, N. Yabuuchi, H. Nakanishi, J. B. Goodenough and Y. Shao-Horn, *Nature chemistry*, 2011, **3**, 546-550.
- D. B. Mitzi, *Progress in Inorganic Chemistry, Volume 48*, 2007, 1-121.
- D. B. Mitzi, C. Feild, W. Harrison and A. Guloy, *Nature*, 1994, **369**, 467-469.
- D. Mitzi, S. Wang, C. Feild, C. Chess and A. Guloy, *Science*, 1995, **267**, 1473-1476.
- C. Kagan, D. Mitzi and C. Dimitrakopoulos, *Science*, 1999, **286**, 945-947.
- X. Hong, T. Ishihara and A. Nurmikko, *Solid state communications*, 1992, **84**, 657-661.
- J.-i. Fujisawa and T. Ishihara, *Physical Review B*, 2004, **70**, 113203.
- Z. Tang and A. M. Guloy, *J Am Chem Soc*, 1999, **121**, 452-453.
- M. A. Green, K. Emery, Y. Hishikawa, W. Warta and E. D. Dunlop, *Progress in Photovoltaics: Research and Applications*, 2012, **20**, 12-20.
- C. Li, X. Lu, W. Ding, L. Feng, Y. Gao and Z. Guo, *Acta Crystallographica Section B: Structural Science*, 2008, **64**, 702-707.
- A. Poglitsch and D. Weber, *The Journal of chemical physics*, 1987, **87**, 6373-6378.
- T. Baikie, Y. Fang, J. M. Kadro, M. Schreyer, F. Wei, S. G. Mhaisalkar, M. Graetzel and T. J. White, *Journal of Materials Chemistry A*, 2013, **1**, 5628-5641.
- J. J. Choi, X. Yang, Z. M. Norman, S. J. Billinge and J. S. Owen, *Nano Lett*, 2013, **14**, 127-133.
- I. Koutselas, L. Ducasse and G. C. Papavassiliou, *Journal of Physics: Condensed Matter*, 1996, **8**, 1217.
- T. Umabayashi, K. Asai, T. Kondo and A. Nakao, *Physical Review B*, 2003, **67**, 155405.
- E. Mosconi, A. Amat, M. K. Nazeeruddin, M. Grätzel and F. De Angelis, *The Journal of Physical Chemistry C*, 2013, **117**, 13902-13913.
- W. J. Yin, T. Shi and Y. Yan, *Adv Mater*, 2014, **26**, 4653-4658.
- H.-S. Kim, C.-R. Lee, J.-H. Im, K.-B. Lee, T. Moehl, A. Marchioro, S.-J. Moon, R. Humphry-Baker, J.-H. Yum and J. E. Moser, *Scientific reports*, 2012, **2**.
- Y. Wang, T. Gould, J. F. Dobson, H. Zhang, H. Yang, X. Yao and H. Zhao, *Phys Chem Chem Phys*, 2014, **16**, 1424-1429.
- J. Even, L. Pedesseau, J.-M. Jancu and C. Katan, *The Journal of Physical Chemistry Letters*, 2013, **4**, 2999-3005.
- P. Umari, E. Mosconi and F. De Angelis, *Scientific reports*, 2014, **4**.
- G. Xing, N. Mathews, S. Sun, S. S. Lim, Y. M. Lam, M. Grätzel, S. Mhaisalkar and T. C. Sum, *Science*, 2013, **342**, 344-347.
- M. M. Lee, J. Teuscher, T. Miyasaka, T. N. Murakami and H. J. Snaith, *Science*, 2012, **338**, 643-647.
- L. Etgar, P. Gao, Z. Xue, Q. Peng, A. K. Chandiran, B. Liu, M. K. Nazeeruddin and M. Grätzel, *J Am Chem Soc*, 2012, **134**, 17396-17399.
- S. D. Stranks, G. E. Eperon, G. Grancini, C. Menelaou, M. J. Alcocer, T. Leijtens, L. M. Herz, A. Petrozza and H. J. Snaith, *Science*, 2013, **342**, 341-344.
- K. Tanaka, T. Takahashi, T. Ban, T. Kondo, K. Uchida and N. Miura, *Solid state communications*, 2003, **127**, 619-623.
- J. Even, L. Pedesseau and C. Katan, *The Journal of Physical Chemistry C*, 2014.
- G. Giorgi, J.-I. Fujisawa, H. Segawa and K. Yamashita, *The Journal of Physical Chemistry Letters*, 2013, **4**, 4213-4216.
- C. Czekelius, M. Hilgendorff, L. Spanhel, I. Bedja, M. Lerch, G. Müller, U. Bloeck, D.-S. Su and M. Giersig, *Adv Mater*, 1999, **11**, 643-646.
- D. E. Gray, *American institute of physics handbook*, McGraw-Hill, 1982.
- C. Wehrenfennig, G. E. Eperon, M. B. Johnston, H. J. Snaith and L. M. Herz, *Adv Mater*, 2014, **26**, 1584-1589.
- W.-J. Yin, T. Shi and Y. Yan, *Appl Phys Lett*, 2014, **104**, 063903.
- X. Lin, J. Wu, X. Lü, Z. Shan, W. Wang and F. Huang, *Phys Chem Chem Phys*, 2009, **11**, 10047-10052.
- X. Lin, F. Huang, W. Wang, Y. Wang, Y. Xia and J. Shi, *Applied Catalysis A: General*, 2006, **313**, 218-223.
- X. Lü, W. Yang, Z. Quan, T. Lin, L. Bai, L. Wang, F. Huang and Y. Zhao, *J Am Chem Soc*, 2013, **136**, 419-426.
- J. Goodenough and J.-S. Zhou, *Chem Mater*, 1998, **10**, 2980-2993.
- J. GOODENOUGH, N. Menyuk, K. Dwight and J. KAFALAS, *Le Journal de Physique Colloques*, 1971, **32**, C1-622-C621-624.
- A. Fujishima, *nature*, 1972, **238**, 37-38.
- T. Lin, C. Yang, Z. Wang, H. Yin, X. Lü, F. Huang, J. Lin, X. Xie and M. Jiang, *Energy & Environmental Science*, 2014, **7**, 967-972.
- Z. Wang, C. Yang, T. Lin, H. Yin, P. Chen, D. Wan, F. Xu, F. Huang, J. Lin and X. Xie, *Energy & Environmental Science*, 2013, **6**, 3007-3014.
- S. Yang, J. Seidel, S. Byrnes, P. Shafer, C.-H. Yang, M. Rossell, P. Yu, Y.-H. Chu, J. Scott and J. Ager, *Nature Nanotechnology*, 2010, **5**, 143-147.
- M. Alexe and D. Hesse, *Nat Commun*, 2011, **2**, 256.

- Journal Name
52. R. Nechache, C. Harnagea, S. Li, L. Cardenas, W. Huang, J. Chakrabartty and F. Rosei, *Nature Photonics*, 2015, **9**, 61-67.
 53. G. Zhang, H. Wu, G. Li, Q. Huang, C. Yang, F. Huang, F. Liao and J. Lin, *Scientific reports*, 2013, **3**.
 54. F. Brivio, A. B. Walker and A. Walsh, *APL Materials*, 2013, **1**, 042111.
 55. J. M. Frost, K. T. Butler, F. Brivio, C. H. Hendon, M. van Schilfgaarde and A. Walsh, *Nano Lett*, 2014, **14**, 2584-2590.
 56. R. Gottesman, E. Haltzi, L. Gouda, S. Tirosh, Y. Bouhadana, A. Zaban, E. Mosconi and F. De Angelis, *The Journal of Physical Chemistry Letters*, 2014, **5**, 2662-2669.
 57. E. J. Juarez-Perez, R. S. Sanchez, L. Badia, G. Garcia-Belmonte, Y. S. Kang, I. Mora-Sero and J. Bisquert, *The Journal of Physical Chemistry Letters*, 2014, **5**, 2390-2394.
 58. Y. Yuan, Z. Xiao, B. Yang and J. Huang, *Journal of Materials Chemistry A*, 2014, **2**, 6027-6041.
 59. C. C. Stoumpos, C. D. Malliakas and M. G. Kanatzidis, *Inorg Chem*, 2013, **52**, 9019-9038.
 60. Y. Kutes, L. Ye, Y. Zhou, S. Pang, B. D. Huey and N. P. Padture, *The Journal of Physical Chemistry Letters*, 2014, **5**, 3335-3339.
 61. Z. Ku, Y. Rong, M. Xu, T. Liu and H. Han, *Scientific reports*, 2013, **3**.
 62. Z. Li, S. A. Kulkarni, P. P. Boix, E. Shi, A. Cao, K. Fu, S. K. Batabyal, J. Zhang, Q. Xiong and L. H. Wong, *ACS nano*, 2014, **8**, 6797-6804.
 63. Q. Jiang, X. Sheng, B. Shi, X. Feng and T. Xu, *The Journal of Physical Chemistry C*, 2014, **118**, 25878-25883.
 64. J.-H. Im, C.-R. Lee, J.-W. Lee, S.-W. Park and N.-G. Park, *Nanoscale*, 2011, **3**, 4088-4093.
 65. G. M. Nature, 2001, **414**, 338-344.
 66. U. Bach, D. Lupo, P. Comte, J. Moser, F. Weissörtel, J. Salbeck, H. Spreitzer and M. Grätzel, *Nature*, 1998, **395**, 583-585.
 67. J. H. Heo, S. H. Im, J. H. Noh, T. N. Mandal, C.-S. Lim, J. A. Chang, Y. H. Lee, H.-j. Kim, A. Sarkar and M. K. Nazeeruddin, *Nature photonics*, 2013, **7**, 486-491.
 68. G. E. Eperon, V. M. Burlakov, P. Docampo, A. Goriely and H. J. Snaith, *Advanced Functional Materials*, 2014, **24**, 151-157.
 69. Q. Chen, H. Zhou, Z. Hong, S. Luo, H.-S. Duan, H.-H. Wang, Y. Liu, G. Li and Y. Yang, *J Am Chem Soc*, 2013, **136**, 622-625.
 70. M. Liu, M. B. Johnston and H. J. Snaith, *Nature*, 2013, **501**, 395-398.
 71. D. Liu and T. L. Kelly, *Nature Photonics*, 2013.
 72. W. A. Laban and L. Etgar, *Energy & Environmental Science*, 2013, **6**, 3249-3253.
 73. A. Mei, X. Li, L. Liu, Z. Ku, T. Liu, Y. Rong, M. Xu, M. Hu, J. Chen and Y. Yang, *Science*, 2014, **345**, 295-298.
 74. O. Malinkiewicz, A. Yella, Y. H. Lee, G. M. Espallargas, M. Graetzel, M. K. Nazeeruddin and H. J. Bolink, *Nature Photonics*, 2014, **8**, 128-132.
 75. J. Seo, S. Park, Y. C. Kim, N. J. Jeon, J. H. Noh, S. C. Yoon and S. I. Seok, *Energy & Environmental Science*, 2014, **7**, 2642-2646.
 76. J. You, Z. Hong, Y. Yang, Q. Chen, M. Cai, T.-B. Song, C.-C. Chen, S. Lu, Y. Liu and H. Zhou, 2014.
 77. P. Docampo, J. M. Ball, M. Darwich, G. E. Eperon and H. J. Snaith, *Nat Commun*, 2013, **4**.
 78. E. Edri, S. Kirmayer, S. Mukhopadhyay, K. Gartsman, G. Hodes and D. Cahen, *Nat Commun*, 2014, **5**.
 79. A. Marchioro, J. Teuscher, D. Friedrich, M. Kunst, R. Van De Krol, T. Moehl, M. Grätzel and J.-E. Moser, *Nature Photonics*, 2014, **8**, 250-255.
 80. E. Edri, S. Kirmayer, A. Henning, S. Mukhopadhyay, K. Gartsman, Y. Rosenwaks, G. Hodes and D. Cahen, *Nano Lett*, 2014, **14**, 1000-1004.
 81. V. Roiati, S. Colella, G. Lerario, L. De Marco, A. Rizzo, A. Listorti and G. Gigli, *Energy & Environmental Science*, 2014, **7**, 1889-1894.
 82. Y. Zhao, A. M. Nardes and K. Zhu, *The Journal of Physical Chemistry Letters*, 2014, **5**, 490-494.
 83. Y. Zhao and K. Zhu, *The Journal of Physical Chemistry Letters*, 2013, **4**, 2880-2884.
 84. A. Abrusci, S. D. Stranks, P. Docampo, H.-L. Yip, A. K.-Y. Jen and H. J. Snaith, *Nano Lett*, 2013, **13**, 3124-3128.
 85. A. Dualah, T. Moehl, N. T éreault, J. Teuscher, P. Gao, M. K. Nazeeruddin and M. Grätzel, *ACS nano*, 2013, **8**, 362-373.
 86. H.-S. Kim, I. Mora-Sero, V. Gonzalez-Pedro, F. Fabregat-Santiago, E. J. Juarez-Perez, N.-G. Park and J. Bisquert, *Nat Commun*, 2013, **4**.
 87. V. Gonzalez-Pedro, E. J. Juarez-Perez, W.-S. Arsyad, E. M. Barea, F. Fabregat-Santiago, I. Mora-Sero and J. Bisquert, *Nano Lett*, 2014, **14**, 888-893.
 88. A. Kojima, M. Ikegami, K. Teshima and T. Miyasaka, *Chemistry Letters*, 2012, **41**, 397-399.
 89. P. Audebert, G. Clavier, V. Alain-Rizzo, E. Deleporte, S. Zhang, J.-S. Lauret, G. Lanty and C. Boissiere, *Chem Mater*, 2009, **21**, 210-214.
 90. L. C. Schmidt, A. Pertegás, S. González-Carrero, O. Malinkiewicz, S. Agouram, G. Mínguez Espallargas, H. J. Bolink, R. E. Galian and J. Pérez-Prieto, *J Am Chem Soc*, 2014, **136**, 850-853.
 91. G. E. Eperon, V. M. Burlakov, A. Goriely and H. J. Snaith, *ACS nano*, 2013, **8**, 591-598.
 92. A. Dualah, N. T éreault, T. Moehl, P. Gao, M. K. Nazeeruddin and M. Grätzel, *Advanced Functional Materials*, 2014, **24**, 3250-3258.
 93. B. Conings, L. Baeten, C. De Dobbelaere, J. D'Haen, J. Manca and H. G. Boyen, *Adv Mater*, 2014, **26**, 2041-2046.
 94. J. Burschka, N. Pellet, S.-J. Moon, R. Humphry-Baker, P. Gao, M. K. Nazeeruddin and M. Grätzel, *Nature*, 2013, **499**, 316-319.
 95. N. Pellet, P. Gao, G. Gregori, T. Y. Yang, M. K. Nazeeruddin, J. Maier and M. Grätzel, *Angewandte Chemie International Edition*, 2014, **53**, 3151-3157.
 96. C. Roldán-Carmona, O. Malinkiewicz, A. Soriano, G. M. Espallargas, A. Garcia, P. Reinecke, T. Kroyer, M. I. Dar, M. K. Nazeeruddin and H. J. Bolink, *Energy & Environmental Science*, 2014, **7**, 994-997.
 97. Q. Chen, H. Zhou, T.-B. Song, S. Luo, Z. Hong, H.-S. Duan, L. Dou, Y. Liu and Y. Yang, *Nano Lett*, 2014, **14**, 4158-4163.
 98. N. J. Jeon, J. H. Noh, W. S. Yang, Y. C. Kim, S. Ryu, J. Seo and S. I. Seok, *Nature*, 2015, **517**, 476-480.
 99. Y. Ogomi, A. Morita, S. Tsukamoto, T. Saitho, N. Fujikawa, Q. Shen, T. Toyoda, K. Yoshino, S. S. Pandey and T. Ma, *The Journal of Physical Chemistry Letters*, 2014, **5**, 1004-1011.
 100. J. H. Noh, S. H. Im, J. H. Heo, T. N. Mandal and S. I. Seok, *Nano Lett*, 2013, **13**, 1764-1769.

101. S. A. Kulkarni, T. Baikie, P. P. Boix, N. Yantara, N. Mathews and S. Mhaisalkar, *Journal of Materials Chemistry A*, 2014, **2**, 9221-9225.
102. G. E. Eperon, S. D. Stranks, C. Menelaou, M. B. Johnston, L. M. Herz and H. J. Snaith, *Energy & Environmental Science*, 2014, **7**, 982-988.
103. E. Edri, S. Kirmayer, M. Kulbak, G. Hodes and D. Cahen, *The Journal of Physical Chemistry Letters*, 2014, **5**, 429-433.
104. N. Kitazawa, Y. Watanabe and Y. Nakamura, *Journal of materials science*, 2002, **37**, 3585-3587.
105. S. Colella, E. Mosconi, P. Fedeli, A. Listorti, F. Gazza, F. Orlandi, P. Ferro, T. Besagni, A. Rizzo and G. Calestani, *Chem Mater*, 2013, **25**, 4613-4618.
106. J. M. Ball, M. M. Lee, A. Hey and H. J. Snaith, *Energy & Environmental Science*, 2013, **6**, 1739-1743.
107. L. Etgar, P. Gao, Z. Xue, Q. Peng, A. K. Chandiran, B. Liu, M. K. Nazeeruddin and M. Grätzel, *J Am Chem Soc*, 2012, **134**, 17396-17399.
108. H.-S. Kim, J.-W. Lee, N. Yantara, P. P. Boix, S. A. Kulkarni, S. Mhaisalkar, M. Grätzel and N.-G. Park, *Nano Lett*, 2013, **13**, 2412-2417.
109. X. S. Qinglong Jiang, Yingxuan Li, Xinjian Feng and Tao Xu, *chem Commun*, 2014.
110. X. Gao, J. Li, J. Baker, Y. Hou, D. Guan, J. Chen and C. Yuan, *Chemical Communications*, 2014, **50**, 6368-6371.
111. S. K. Pathak, A. Abate, P. Ruckdeschel, B. Roose, K. C. Gödel, Y. Vaynzof, A. Santhala, S. I. Watanabe, D. J. Hollman and N. Noel, *Advanced Functional Materials*, 2014.
112. P. Qin, A. L. Domanski, A. K. Chandiran, R. Berger, H.-J. Butt, M. I. Dar, T. Moehl, N. Tetreault, P. Gao and S. Ahmad, *Nanoscale*, 2014, **6**, 1508-1514.
113. Z. Zhu, J. Ma, Z. Wang, C. Mu, Z. Fan, L. Du, Y. Bai, L. Fan, H. Yan and D. L. Phillips, *J Am Chem Soc*, 2014, **136**, 3760-3763.
114. M. H. Kumar, N. Yantara, S. Dharani, M. Graetzel, S. Mhaisalkar, P. P. Boix and N. Mathews, *Chemical Communications*, 2013, **49**, 11089-11091.
115. D.-Y. Son, J.-H. Im, H.-S. Kim and N.-G. Park, *The Journal of Physical Chemistry C*, 2014, **118**, 16567-16573.
116. J. Y. Jeng, Y. F. Chiang, M. H. Lee, S. R. Peng, T. F. Guo, P. Chen and T. C. Wen, *Adv Mater*, 2013, **25**, 3727-3732.
117. E. J. Juarez-Perez, M. Wüßler, F. Fabregat-Santiago, K. Lakus-Wollny, E. Mankel, T. Mayer, W. Jaegermann and I. Mora-Sero, *The Journal of Physical Chemistry Letters*, 2014, **5**, 680-685.
118. N. J. Jeon, H. G. Lee, Y. C. Kim, J. Seo, J. H. Noh, J. Lee and S. I. Seok, *J Am Chem Soc*, 2014, **136**, 7837-7840.
119. Y. Guo, C. Liu, K. Inoue, K. Harano, H. Tanaka and E. Nakamura, *J. Mater. Chem. A*, 2014, **2**, 13827-13830.
120. F. Di Giacomo, S. Razza, F. Matteocci, A. D'Epifanio, S. Licoccia, T. M. Brown and A. Di Carlo, *Journal of Power Sources*, 2014, **251**, 152-156.
121. D. Bi, L. Yang, G. Boschloo, A. Hagfeldt and E. M. Johansson, *The Journal of Physical Chemistry Letters*, 2013, **4**, 1532-1536.
122. R. Schölin, M. H. Karlsson, S. K. Eriksson, H. Siegbahn, E. M. Johansson and H. Rensmo, *The Journal of Physical Chemistry C*, 2012, **116**, 26300-26305.
123. W. H. Nguyen, C. D. Bailie, E. L. Unger and M. D. McGehee, *J Am Chem Soc*, 2014, **136**, 10996-11001.
124. G. V. Tormos, M. G. Bakker, P. Wang, M. Lakshmikantham, M. P. Cava and R. M. Metzger, *J Am Chem Soc*, 1995, **117**, 8528-8535.
125. J. Liu, Y. Wu, C. Qin, X. Yang, T. Yasuda, A. Islam, K. Zhang, W. Peng, W. Chen and L. Han, *Energy & Environmental Science*, 2014, **7**, 2963-2967.
126. H. Li, K. Fu, A. Hagfeldt, M. Grätzel, S. G. Mhaisalkar and A. C. Grimsdale, *Angewandte Chemie International Edition*, 2014, **53**, 4085-4088.
127. P. Qin, H. Kast, M. K. Nazeeruddin, S. M. Zakeeruddin, A. Mishra, P. Bärle and M. Grätzel, *Energy & Environmental Science*, 2014, **7**, 2981-2985.
128. P. Qin, S. Paek, M. I. Dar, N. Pellet, J. Ko, M. Grätzel and M. K. Nazeeruddin, *J Am Chem Soc*, 2014, **136**, 8516-8519.
129. J. A. Christians, R. C. Fung and P. V. Kamat, *J Am Chem Soc*, 2013, **136**, 758-764.
130. A. S. Subbiah, A. Halder, S. Ghosh, N. Mahuli, G. Hodes and S. K. Sarkar, *The Journal of Physical Chemistry Letters*, 2014, **5**, 1748-1753.
131. S. D. Chavhan, O. Miguel, H. J. Grande, V. Gonzalez-Pedro, R. S. Sánchez, E. M. Barea, I. Mora-Seró and T.-Z. Ramon, *Journal of Materials Chemistry A*, 2014, **2**, 12754-12760.
132. P. Qin, S. Tanaka, S. Ito, N. Tetreault, K. Manabe, H. Nishino, M. K. Nazeeruddin and M. Grätzel, *Nat Commun*, 2014, **5**.
133. Z. Zhu, Y. Bai, T. Zhang, Z. Liu, X. Long, Z. Wei, Z. Wang, L. Zhang, J. Wang and F. Yan, *Angewandte Chemie*, 2014, **126**, 1-6.
134. K.-C. Wang, J.-Y. Jeng, P.-S. Shen, Y.-C. Chang, E. W.-G. Diau, C.-H. Tsai, T.-Y. Chao, H.-C. Hsu, P.-Y. Lin and P. Chen, *Scientific reports*, 2014, **4**.
135. L. Hu, J. Peng, W. Wang, Z. Xia, J. Yuan, J. Lu, X. Huang, W. Ma, H. Song and W. Chen, *ACS Photonics*, 2014, **1**, 547-553.
136. Z. Wu, S. Bai, J. Xiang, Z. Yuan, Y. Yang, W. Cui, X. Gao, Z. Liu, Y. Jin and B. Sun, *Nanoscale*, 2014, **6**, 10505-10510.
137. J. Bisquert, *Phys Chem Chem Phys*, 2003, **5**, 5360-5364.
138. J. A. del Cueto, C. Deline, D. Albin, S. Rummel and A. Anderberg, *SPIE Solar Energy+ Technology*, 2009.
139. M. Herman, M. Jankovec and M. Topič, *International Journal of Photoenergy*, 2012, **2012**.
140. H. J. Snaith, A. Abate, J. M. Ball, G. E. Eperon, T. Leijtens, N. K. Noel, S. D. Stranks, J. T.-W. Wang, K. Wojciechowski and W. Zhang, *The Journal of Physical Chemistry Letters*, 2014, **5**, 1511-1515.
141. E. Unger, E. Hoke, C. Bailie, W. Nguyen, A. Bowring, T. Heumüller, M. Christoforo and M. McGehee, *Energy & Environmental Science*, 2014, **7**, 3690-3698.
142. H.-S. Kim and N.-G. Park, *The Journal of Physical Chemistry Letters*, 2014, **5**, 2927-2934.
143. J. Wei, Y. Zhao, H. Li, G. Li, J. Pan, D. Xu, Q. Zhao and D. Yu, *The Journal of Physical Chemistry Letters*, 2014, **5**, 3937-3945.
144. R. S. Sanchez, V. Gonzalez-Pedro, J.-W. Lee, N.-G. Park, Y. S. Kang, I. Mora-Sero and J. Bisquert, *The Journal of Physical Chemistry Letters*, 2014, **5**, 2357-2363.
145. J. Bisquert, L. Bertoluzzi, I. Mora-Sero and G. Garcia-Belmonte, *The Journal of Physical Chemistry C*, 2014, **118**, 18983-18991.

Journal Name

146. H.-W. Chen, N. Sakai, M. Ikegami and T. Miyasaka, *The Journal of Physical Chemistry Letters*, 2014.
147. *Science*, 2013, **342**, 794-797.
148. http://www.nrel.gov/ncpv/images/efficiency_chart.jpg.
149. H. J. Snaith, *The Journal of Physical Chemistry Letters*, 2013, **4**, 3623-3630.
150. G. Niu, X. Guo and L. Wang, *Journal of Materials Chemistry A*, 2015.
151. F. Hao, C. C. Stoumpos, D. H. Cao, R. P. Chang and M. G. Kanatzidis, *Nature Photonics*, 2014, **8**, 489-494.